CRREL
REPORT 87-20

US Army Corps of Engineers
Cold Regions Research & Engineering Laboratory

Microwave and structural properties of saline ice

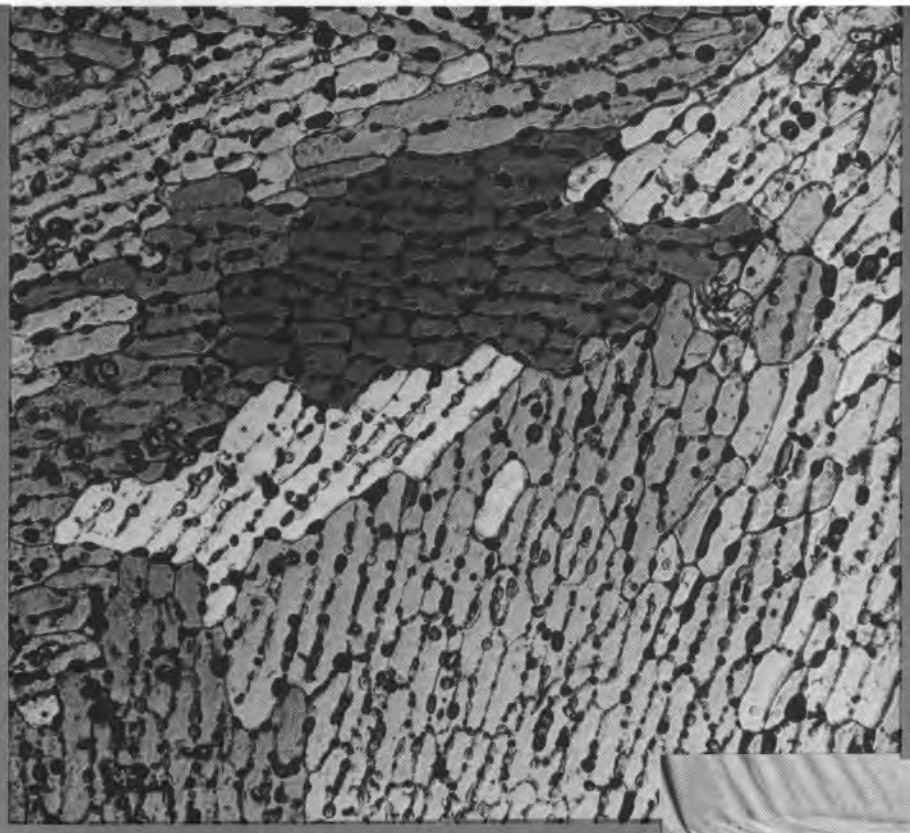

CRREL Report 87-20

October 1987

Microwave and structural properties of saline ice

Anthony J. Gow, Steven A. Arcone and Seth G. McGrew

Prepared for
OFFICE OF NAVAL RESEARCH

UNCLASSIFIED
SECURITY CLASSIFICATION OF THIS PAGE

REPORT DOCUMENTATION PAGE

Form Approved
OMB No. 0704-0188
Exp. Date: Jun 30, 1986

1a. REPORT SECURITY CLASSIFICATION
Unclassified

1b. RESTRICTIVE MARKINGS

2a. SECURITY CLASSIFICATION AUTHORITY

2b. DECLASSIFICATION / DOWNGRADING SCHEDULE

3. DISTRIBUTION / AVAILABILITY OF REPORT
Approved for public release; distribution is unlimited.

4. PERFORMING ORGANIZATION REPORT NUMBER(S)
CRREL Report 87-20

5. MONITORING ORGANIZATION REPORT NUMBER(S)

6a. NAME OF PERFORMING ORGANIZATION
U.S. Army Cold Regions Research and Engineering Laboratory

6b. OFFICE SYMBOL (If applicable)
CECRL

7a. NAME OF MONITORING ORGANIZATION
Office of Naval Research

6c. ADDRESS (City, State, and ZIP Code)
Hanover, New Hampshire 03755-1290

7b. ADDRESS (City, State, and ZIP Code)
Arlington, Virginia 22217

8a. NAME OF FUNDING / SPONSORING ORGANIZATION

8b. OFFICE SYMBOL (If applicable)

9. PROCUREMENT INSTRUMENT IDENTIFICATION NUMBER
N000148W RM24001

8c. ADDRESS (City, State, and ZIP Code)

10. SOURCE OF FUNDING NUMBERS

PROGRAM ELEMENT NO.	PROJECT NO.	TASK NO.	WORK UNIT ACCESSION NO

11. TITLE (Include Security Classification)
Microwave and Structural Properties of Saline Ice

12. PERSONAL AUTHOR(S)
Gow, Anthony J., Arcone, Steven A. and McGrew, Seth G.

13a. TYPE OF REPORT	13b. TIME COVERED FROM ____ TO ____	14. DATE OF REPORT (Year, Month, Day)	15. PAGE COUNT
		October 1987	41

16. SUPPLEMENTARY NOTATION

17. COSATI CODES		
FIELD	GROUP	SUB-GROUP

18. SUBJECT TERMS (Continue on reverse if necessary and identify by block number)
Dielectric properties
Microwave properties
Sea ice
Structural properties

19. ABSTRACT (Continue on reverse if necessary and identify by block number)

The structure and salinity characteristics of saline ice slabs removed from ice sheets grown in an outdoor pool have been studied and related to the complex relative dielectric permittivity measured with free-space transmission techniques at 4.80 and 9.50 GHz. The saline ice closely simulated arctic sea ice in its structural and salinity characteristics, which were regularly monitored in a number of ice sheets grown during the winters of 1983-84 and 1984-85. In-situ transmission measurements at similar frequencies were also made on the ice sheets themselves using antennas located above and beneath the ice. The slab measurements were made during warming from -29° to -2°C on slabs grown during the winter of 1983-84 (4.75 GHz) and during a warming and cooling cycle over a slightly larger temperature range on slabs grown during the winter of 1984-85 (4.80 and 9.50 GHz). The 1983-84 results show both the real ε_r' and imaginary ε_r'' parts to vary almost in direct proportion to the brine volume v_B at values lower than about 50°/oo. The 1984-85 slabs showed only ε_r' to depend strongly on v_B while values of ε_r'' were considerably lower than in the previous year. This difference may have been caused by greater electrical conductivity in the 1983-84 slabs, which could be related to distinct differences

20. DISTRIBUTION / AVAILABILITY OF ABSTRACT
☒ UNCLASSIFIED/UNLIMITED ☐ SAME AS RPT. ☐ DTIC USERS

21. ABSTRACT SECURITY CLASSIFICATION
Unclassified

22a. NAME OF RESPONSIBLE INDIVIDUAL
Anthony J. Gow

22b. TELEPHONE (Include Area Code)
603-646-4100

22c. OFFICE SYMBOL
CECRL-RS

DD FORM 1473, 84 MAR

83 APR edition may be used until exhausted
All other editions are obsolete

SECURITY CLASSIFICATION OF THIS PAGE
UNCLASSIFIED

19. Abstract (cont'd).

seen in brine pocket structure between the years. Values of ε_r' as a function of v_B were slightly lower on the average at 9.50 GHz than at 4.80, and most values of ε_r' agreed with the results of others when their temperature and salinity values were converted to values of v_B. Changes in ε_r' due to thermal modification (laboratory warming) seem more strongly related to a gain in air volume from brine drainage than to the redistribution of brine inclusions. The in-situ measurements showed extremely high attenuation for the young (< 12 cm) brine-rich ice. Good agreement was found between data for the more desalinated samples and the theoretical values predicted by a previously proposed dielectric mixing model. This model was modified by accounting for the brine pocket geometry observed in thin sections, and also by including a bulk conductivity term to account for the observed loss.

PREFACE

This report was prepared by Dr. Anthony J. Gow, Dr. Steven A. Arcone, and Seth G. McGrew of the Snow and Ice Branch, Research Division, U.S. Army Cold Regions Research and Engineering Laboratory.

This work was performed as part of a saline ice research program conducted for the Office of Naval Research (ONR) under Contract No. N000148WRM24001.

The assistance of Allan Delaney in many aspects of this project is gratefully appreciated.

CONTENTS

ILLUSTRATIONS

TABLES

Microwave and Structural Properties of Saline Ice

ANTHONY J. GOW, STEVEN A. ARCONE AND SETH G. MCGREW

Part I. Structural Properties

INTRODUCTION

Despite widespread imaging of sea ice in the Arctic and Antarctic by various remote sensing techniques, only limited attempts have been made to obtain precise correlation of the electrical properties of sea ice with its structural and salinity characteristics. Such correlations (or calibrations) can be accomplished either by conducting ground truth measurements simultaneously with imaging overflights or by performing similar scale model tests on simulated sea ice grown in a test tank or pool. To this end, an outdoor pool was constructed at the U.S. Army Cold Regions Research and Engineering Laboratory (CRREL) and a multidisciplinary investigation undertaken to examine the effect of the salinity and structural characteristics of sea ice on reflectivity and emissivity properties. The purpose of Part I of this report is to document the salinity and structural characteristics of the simulated sea ice (saline ice) used for making measurements of dielectric properties under carefully controlled conditions in the laboratory. Results of the dielectric measurements are reported by Arcone and McGrew in Part II of this report—*Microwave Properties*. This report is based in part on results presented by Arcone and McGrew (1985) and Gow (1985) at the 1985 International Geoscience and Remote Sensing Symposium (IGARSS '85) held at the University of Massachusetts, Amherst.

EXPERIMENTAL SET-UP

Ice sheets were grown in a pool, measuring 12.2×5.2 m, that was excavated to a maximum depth of 1.5 m and covered with a thick neoprene liner (Fig. 1). Concrete pavers were emplaced around the edge of the pool to serve as a work pad. The rest of the facility consisted of a large tent that could be rolled on and off the pool as weather conditions dictated, and a refrigeration unit that was used primarily to offset any melting of the ice during periods of elevated surface air temperature. A space heater was also installed to suppress excessive ice growth during periods of very cold weather. Other investigations concurrent with CRREL's efforts (Grenfell and Comiso 1986, Swift et al. 1986) utilized remote sensing antennas and other instruments mounted on a steel gantry that spanned the pool and could be moved across the pavers to permit imaging measurements on any part of the ice sheet. In total, personnel from the Universities of Kansas, Washington, Massachusetts and Wisconsin, the Environmental Research Institute of Michigan (ERIM), Massachusetts Institute of Technology, NASA and the U.S. Navy laboratories, NORDA and NUSC, also participated in the experiments that included radiometer, radar and acoustical backscatter and dielectric property measurements.

The pool was filled with water that was raised to the desired salinity (23–25‰) by adding granulated sea salt and mixing it thoroughly with circulating pumps.

Full-scale testing was begun on 19 December 1983 when the pool was allowed to freeze spontaneously without seeding. Growth of this ice sheet resulted in the formation of massive prismatic crystals with c-axes that reverted slowly to horizontal orientations at the bottom. At this scale such ice does not accurately reflect the textures of naturally frozen sea water. Accordingly, this ice sheet was broken up and the blocks entirely removed in readiness for a second ice sheet. On 17 January 1984, the surface of the pool was spray

a. Tent used to cover pond.

b. Experimental ice sheet with tent rolled off.

Figure 1. Saline ice test facility at CRREL.

seeded in an attempt to stimulate growth of more typically columnar ice crystals. This technique, previously employed by the Gow (1986) to promote columnar crystal growth in simulated freshwater ice, also succeeded for the saline water in the pool. The resultant ice sheet was allowed to continue growing for 36 days of testing during which the structural and salinity characteristics were monitored at regular intervals. The crystalline texture of the ice at all stages of its growth was found to closely scale that of normal congelation ice. Congelation ice forms by direct freezing of sea

water to the underside of the sheet; such a process typically yields vertically elongated crystals with their c-axes oriented substantially in the horizontal plane (Weeks and Ackley 1982).

Experiments were continued on an expanded scale during the 1984-85 winter when three ice sheets were grown and tested. These included one ice sheet that was divided into seeded and unseeded portions, and two seeded ice sheets, the final one of which we succeeded in converting into a sheet with structural and salinity properties transitional to those of second-year ice.

ANALYTICAL TECHNIQUES

Once freezing had begun, each ice sheet was monitored closely for salinity and structure throughout its entire growth history. To limit the effects of brine drainage, salinity measurements were usually made on specimens prepared on site as soon as a sample was sawed or cored from the ice sheet. Often additional measurements were run on a second core or sample to determine if salinity differed significantly on different parts of an ice sheet. Results of these measurements generally agreed within 0.3‰ at corresponding levels in the ice sheet. Salinities were measured with a Beckman Solubridge RB-5 that was frequently calibrated against solutions prepared from Copenhagen Standard Seawater (chlorinity = 19.373‰). The precision of these measurements was estimated at ±0.2‰. Data were either plotted conventionally as a function of depth or as cumulative depth (depth × salinity) values vs depth.

Crystal structure studies were made with the aid of thin sections cut vertically and horizontally from blocks sawn from the ice sheet, thereby furnishing a three-dimensional view of model sea ice structure. Sections were prepared on a histological microtome adapted for use with ice. Details of this technique as applied to sea ice are given in Gow and Weeks (1977). Sections were sliced to a thickness of 0.5 mm or less and then photographed between crossed Polaroids at two magnifications: at natural (1:1) scale with a 10- × 12.5-cm press camera and at 7× magnification with a 12.5- × 17.5-cm bellows extension camera. The latter format yields large photos for examining the finer details of ice platelet and brine inclusion characteristics in individual saline ice crystals.

RESULTS AND DISCUSSION

The natural freezing of seawater generally leads to growth of vertically elongated columnar crystals in sheets that reach 2 m or so in thickness. Closer inspection of the columnar crystals invariably reveals a substructure of long, vertical plates separated by parallel layers of brine inclusions (see Fig. 2). Such vertical sandwich substructure reflects the process by which excess brine at the ice/water interface is systematically incorporated into the ice. The spacing of these plates (plate width) can vary from a few tenths of a millimeter to 1 mm and depends mainly on the speed of growth; the faster the freezing, the narrower the plate spacing and the greater the salinity. Subsequent changes in this substructure occur mainly in response to temperature changes in the ice. Brine inclusions are particularly sensitive in this regard. Even small changes in thermal regime, resulting from day-to-day changes in surface air temperatures, can lead to significant changes in the geometry of the inclusions and the concentration of the entrapped brine.

1983–84 experiments

Salinity and structure characteristics of the seeded ice sheet are documented in Figures 3 through 6. Magnified sections of crystal substructure in Figure 6 show how well this simulated sea ice matches the naturally frozen product (Fig. 2). This ice sheet had attained a thickness of 32.5 cm before measurements were terminated on 22 February 1984, 36 days after ice growth was initiated. A maximum bulk salinity of 8‰ was measured at the end of three days of growth (see Fig. 3), with salinities then falling progressively to 4‰ after 20 days of growth and to 2‰ after 36 days. This desalination, particularly that for the interval between 20 and 36 days, can be correlated with periods of elevated air temperature that led to flooding and refreezing of 5 cm of freshwater on top of the ice sheet during the latter stages of the experiment. These changes are also demonstrated in the cumulative salinity profiles presented in Figure 3b.

Figure 4 shows the overall nature of the in-situ ice structure observed in vertical and horizontal thin sections of 15-day-old ice photographed between crossed Polaroids. Note the columnar texture of crystals in the vertical section (some of

Figure 2. Horizontal thin section of arctic sea ice, showing crystal substructure composed of ice platelets and brine layers. The crystallographic c-axis (arrow) lies in the plane of the section and is oriented normal to the platy structure of individual crystals. Scale subdivisions are 1 mm.

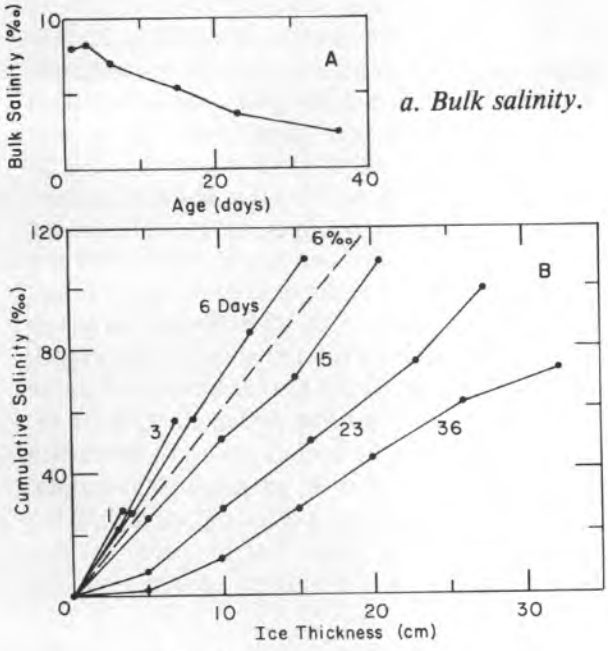

a. Bulk salinity.

b. Cumulative salinity.

Figure 3. Bulk salinity and cumulative salinity (salinity × ice thickness increment) measured as a function of the age and thickness of the ice, respectively. The ice sheet was grown during January and February 1984. In b the profile for an ice sheet growing with a uniform salinity of 6‰ is shown for comparison.

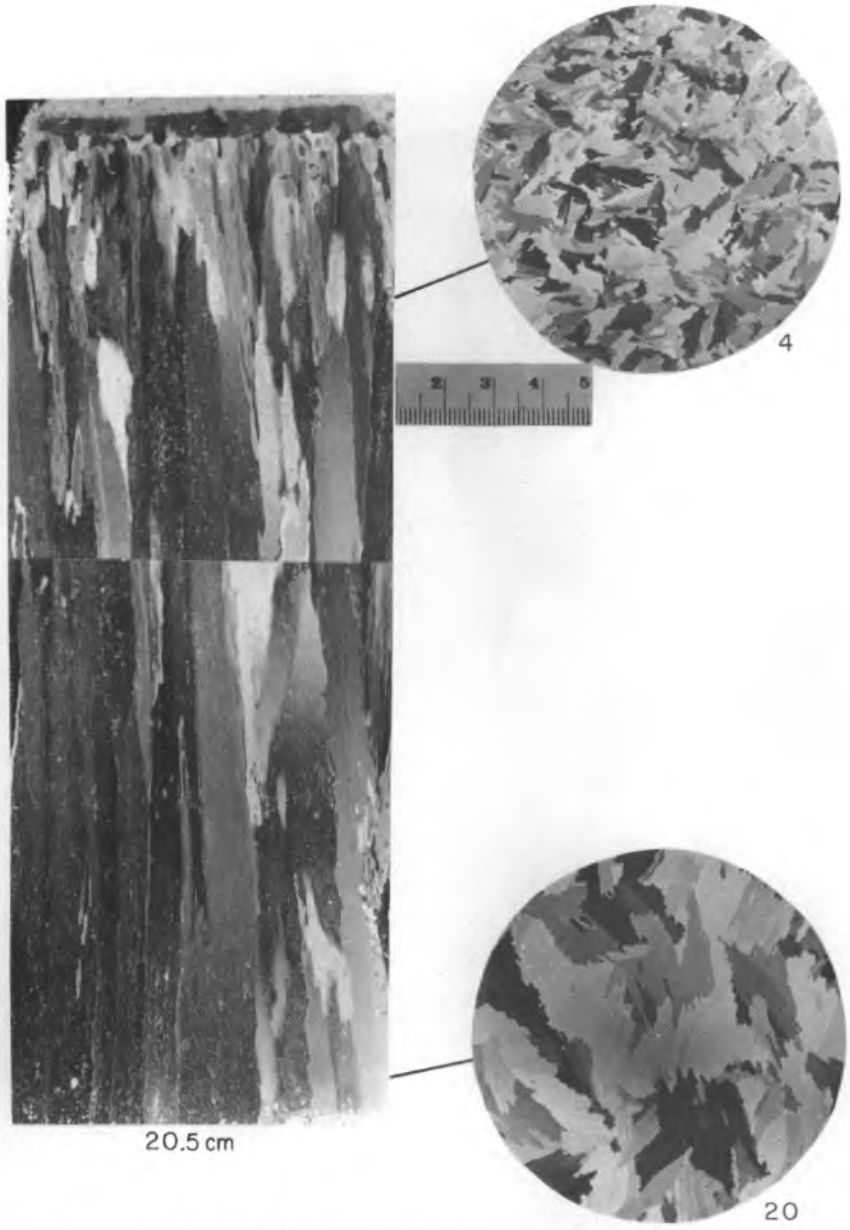

Figure 4. Vertical and horizontal thin sections of structure of ice sheet from which slabs 84-3 and 84-4 were obtained. Scale subdivisions on photographs are 1 mm.

these crystals extend through nearly the entire thickness of ice, 20.5 cm), and the substantial increase in the cross-sectional dimensions of crystals with increasing ice thickness. Such structures, both vertical and horizontal, are indistinguishable from those observed in normal congelation sea ice (Gow and Weeks 1977, Weeks and Ackley 1982). The interpenetrated, feathery appearance of crystals in horizontal sections is also a characteristic feature of congelation sea ice. Though difficult to see at the reduced magnification of the photographs presented in Figure 4, layers of brine inclusions are clearly evident in the thin sections themselves. The bulk salinity of this ice was 5.3‰.

At the time this ice was being sampled for structural and salinity measurements, two slabs, each measuring $46 \times 46 \times 20.8$ cm thick, were removed from the sheet and transferred to a -30°C cold-room in preparation for dielectric measurements (Arcone and McGrew 1985). These measurements were obtained to determine the effect on the dielectric properties of changes in temperature, sa-

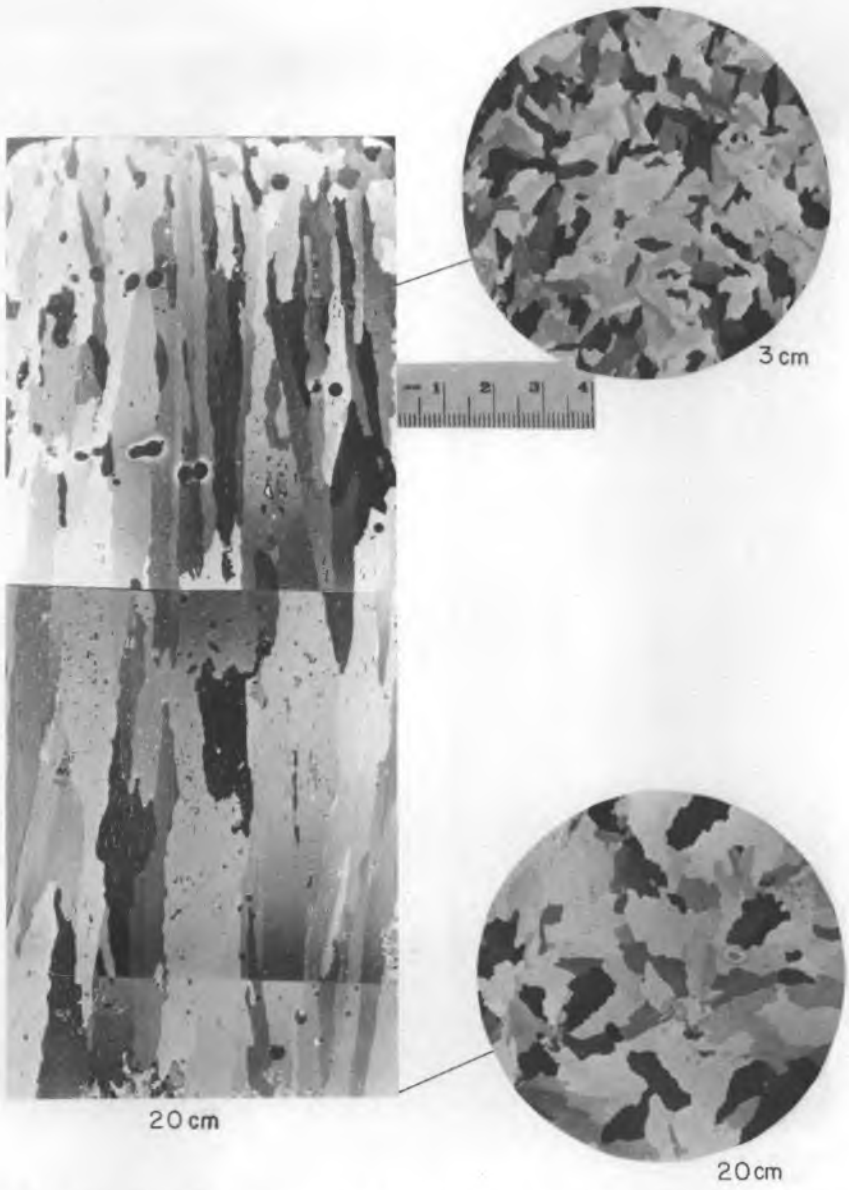

Figure 5. Vertical and horizontal thin section structure in thermally modified ice slab 84-3. Scale subdivisions are 1 mm.

linity and crystal structure of the slabs as they are progressively warmed from -30° to -2 °C. The in-situ salinity of the slabs (here designated as 84-3 and 84-4) averaged 5.3‰. However, brine drainage, following removal of the slabs from the pool, had reduced their bulk salinities to 3.8‰ immediately prior to testing. By the time the temperature of each slab had increased to -2 °C, the salinities of both had further decreased to between 3.3 and 3.2‰. This represents a real loss of brine from the ice, most of which occurs near the melting point.

The effect of this brine loss is to increase porosity, which in the case of slab 84-3, amounted to a 4% increase, as determined by density measurements made prior to and at the end of testing. However, the volume of brine in the ice slab actually increases during warm-up because of eutectic melting of the ice around the brine pockets. This melting in turn leads to progressive enlargement of the pockets, which begin to coalesce at temperatures of around -5 °C, ultimately forming drainage tubules near the melting point. This mobilization and increase in volume of brine, together with partial drainage of brine near the melting point (as described above), is entirely consistent with the explanations given by Arcone and McGrew (Part II,

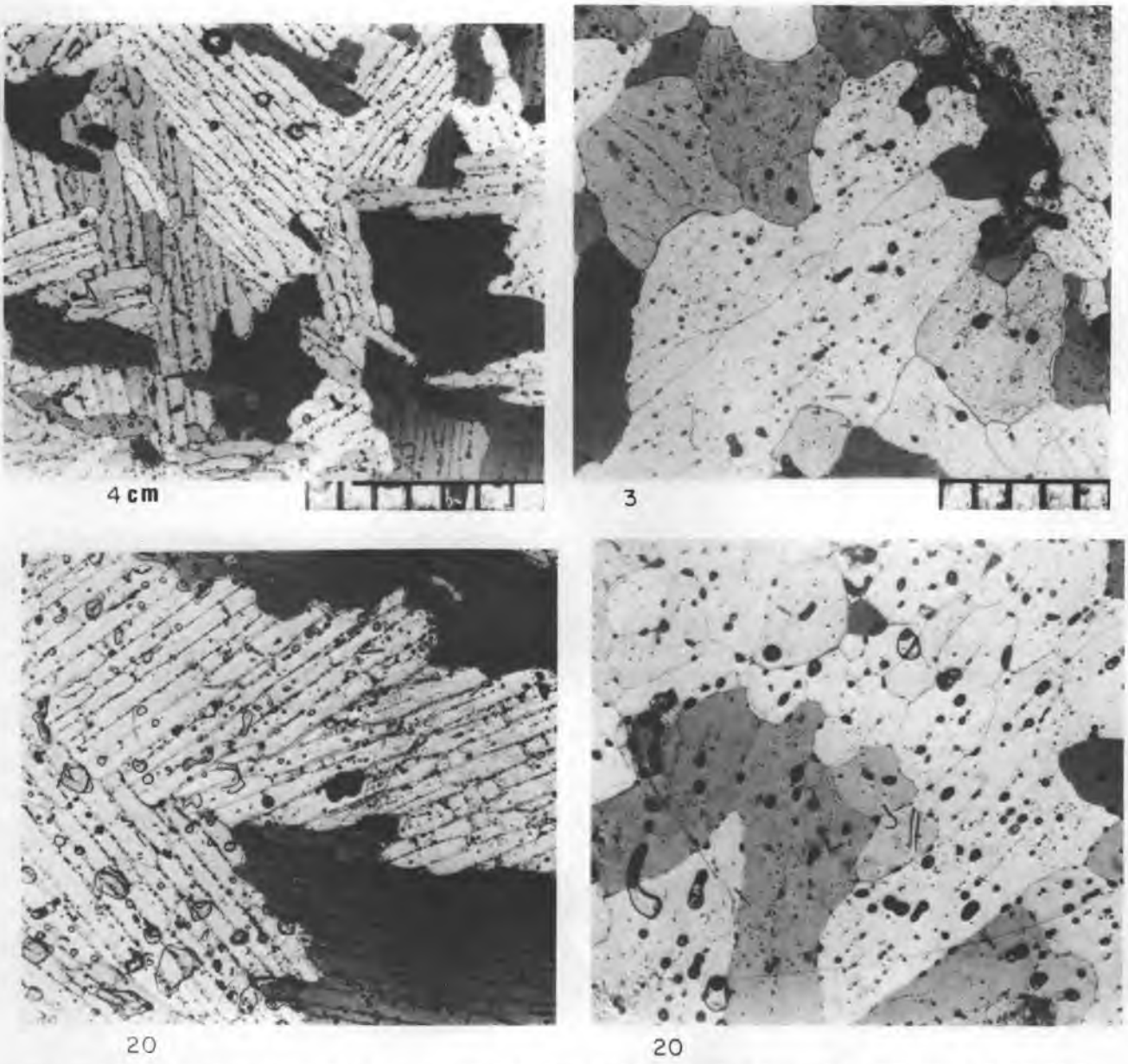

Figure 6. Magnified sections of ice structure (left) before and (right) after thermal modification of slab 84-3. Scale subdivisions are 1 mm.

this report) to account for the observed changes in the dielectric behavior of slabs 84-3 and 84-4 as they underwent warming from -30 °C to -2 °C.

The structural condition of the thermally modified ice in slab 84-3 is shown in Figure 5. The structure departs appreciably from that observed in the sample of in-situ ice (Fig. 4). While the elongated texture of crystals in the thermally modified ice is still retained in vertical sections, crystal boundaries in the horizontal sections have become rounded and the brine inclusion pattern can be seen to have undergone major changes when viewed at higher magnification alongside sections from corresponding depths in the in-situ unmodified ice (Fig.6). Crystals in the unmodified ice exhibit sharply defined ice plate/brine layer substructure. Note that the brine layers in this ice actually consist of strings of inclusions, whereas the brine layers in the thermally conditioned ice have been substantially eliminated and replaced by large bubble-like inclusions and drainage channels. This situation applies equally well to ice obtained near the top and the bottom of the ice sheet. Although these changes in crystal substruc-

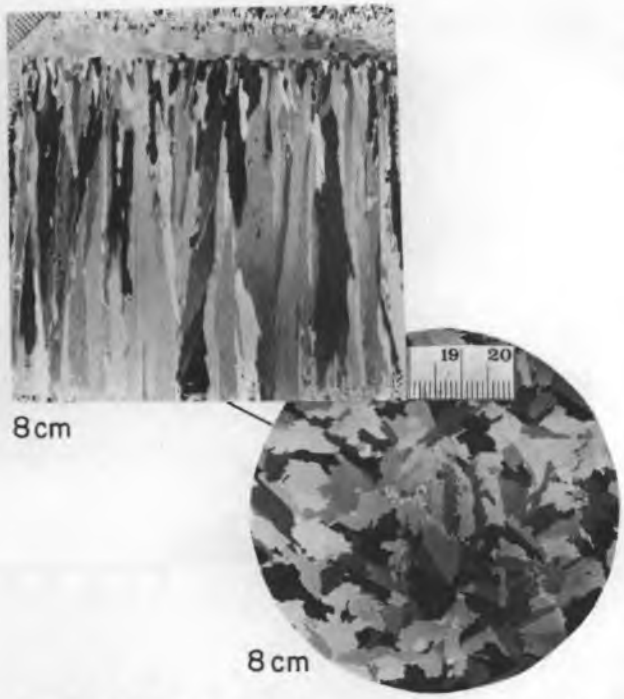

Figure 7. Vertical and horizontal thin sections of seeded ice structure in slab 85-1 prior to microwave testing and thermal modification. Smallest subdivisions are 1 mm.

ture were induced by progressive warming of the sample in the laboratory, essentially identical changes in brine inclusion geometry, salinity characteristics and crystal boundary shape were observed in the ice sheet in the outdoor pool after it had been subjected to several days of above-freezing air temperatures toward the end of the experiment.

1984–85 experiments

Experimental measurements of dielectric properties of ice slabs were extended to samples taken from two of three ice sheets grown during the 1984–85 winter. A total of four slabs were tested under essentially the same conditions as the 1983–84 slabs; that is, samples were stored for some time at −30 °C before beginning microwave transmission measurements. In addition, tests were repeated in reverse to evaluate the nature of the dielectric response as the slabs were cooled from −2° to −30 °C. Results of these measurements substantially confirm the 1983–84 data and are discussed in detail by Arcone and McGrew in Part II of this report.

Slabs designated 85-1 and 85-2 were obtained from seeded and unseeded parts, respectively, of

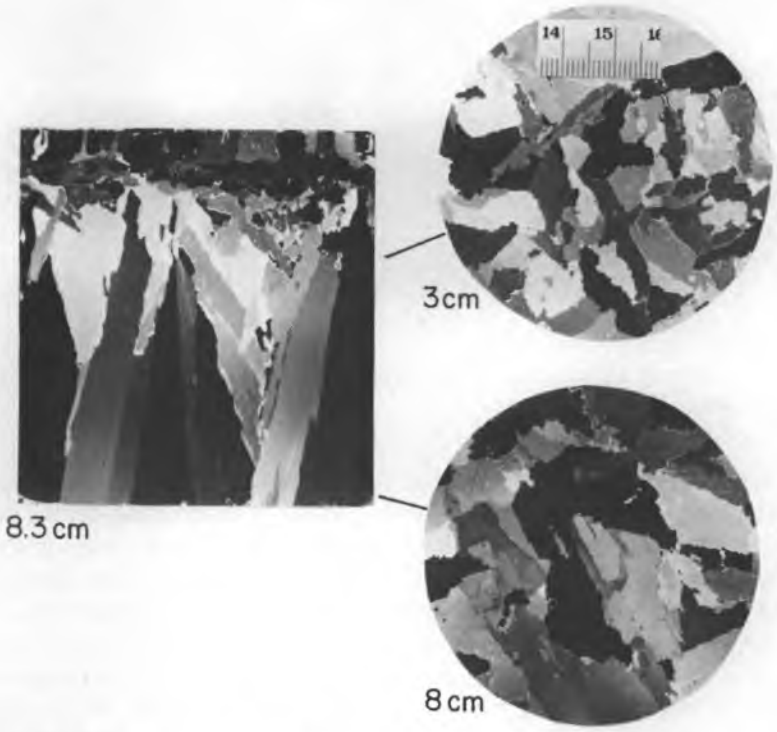

Figure 8. Vertical and horizontal thin sections showing original structure of unseeded ice in slab 85-2. Smallest scale subdivisions are 1 mm.

the same ice sheet. This ice sheet was sampled on 7 January 1985 when 8.5 cm thick. In-situ bulk salinities of 8.3‰ for slab 85-1 and 8.4‰ for slab 85-2 were measured. Significant drainage of brine occurred during sampling and storage of both samples, salinities having decreased to 4.8‰ prior to testing 85-1, and to 5.5‰ in the case of 85-2. At the end of testing, salinities had further decreased to 3.1‰ for 85-1 and to 4.4‰ for 85-2.

Vertical and horizontal thin-section photographs of original (thermally unmodified) ice structure in 85-1 and 85-2, prior to testing, are presented in Figures 7 and 8. The two ice types are both characterized by a sharp transition from a 7-mm layer of c-axis vertical crystals to columnar c-axis horizontal crystals which are very much larger in the unseeded (85-2) slab than in the seeded slab (85-1). However, the congelation crystals of both slabs feature the same platelet/brine layer substructure. Plate widths average 0.7 mm in 85-1 but are only about 0.5 mm in 85-2. The extent to which the substructure of crystals in both slabs has become degraded during testing is indicated in Figures 9 and 10. Most of the substructure in the

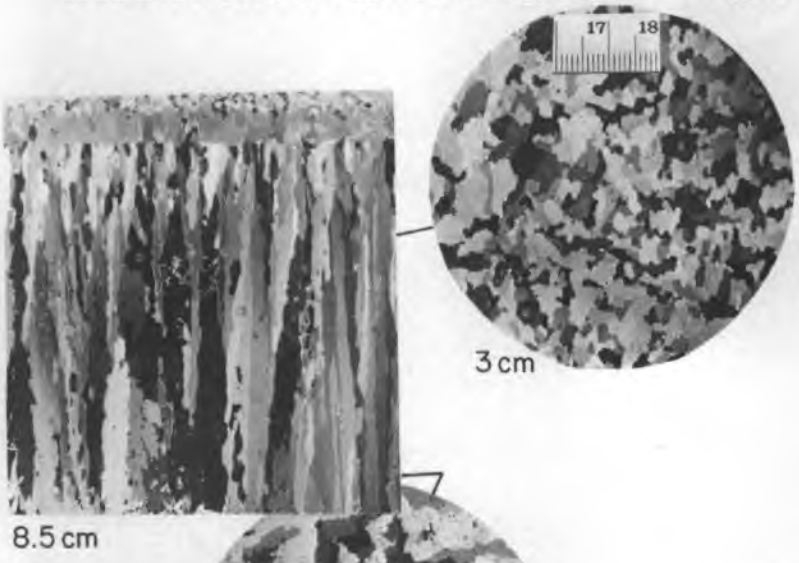

Figure 9. Vertical and horizontal thin section structure in thermally modified ice slab 85-1. Smallest scale subdivisions are 1 mm.

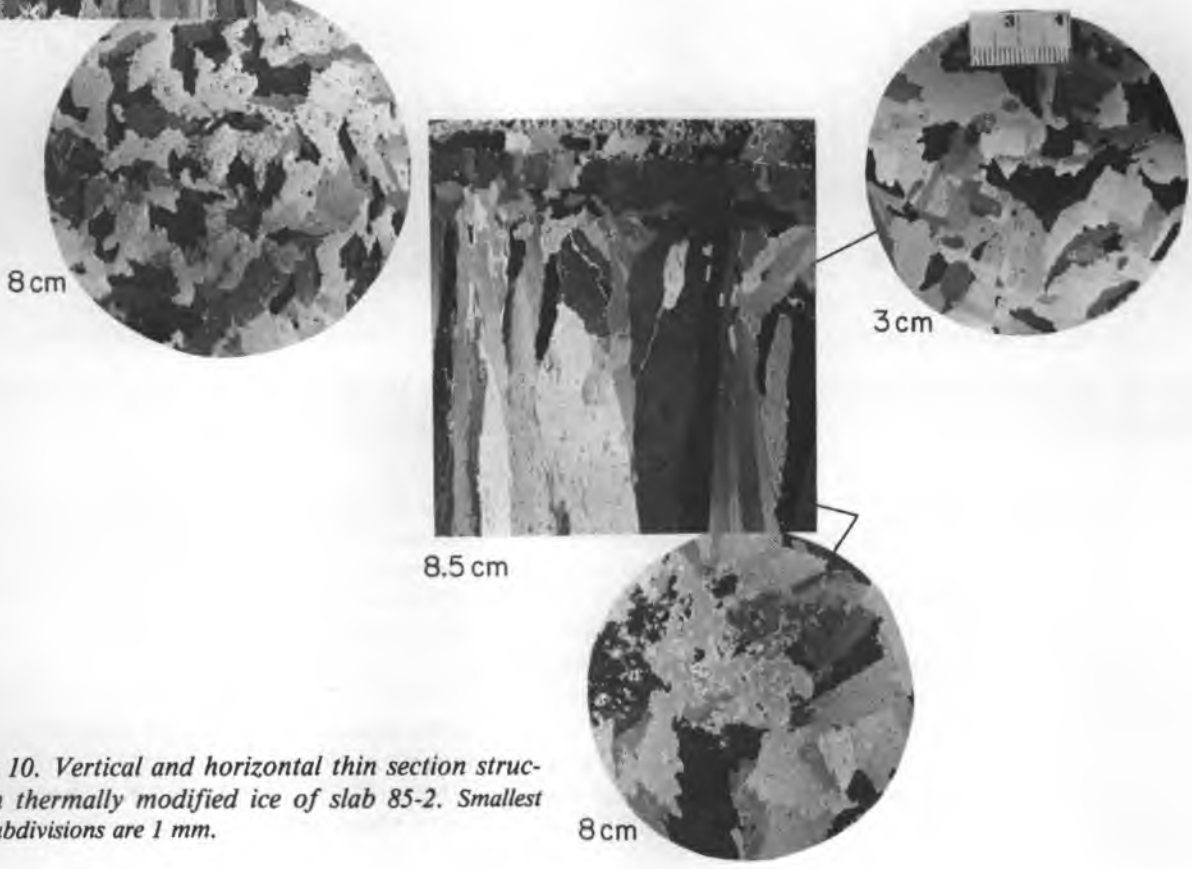

Figure 10. Vertical and horizontal thin section structure in thermally modified ice of slab 85-2. Smallest scale subdivisions are 1 mm.

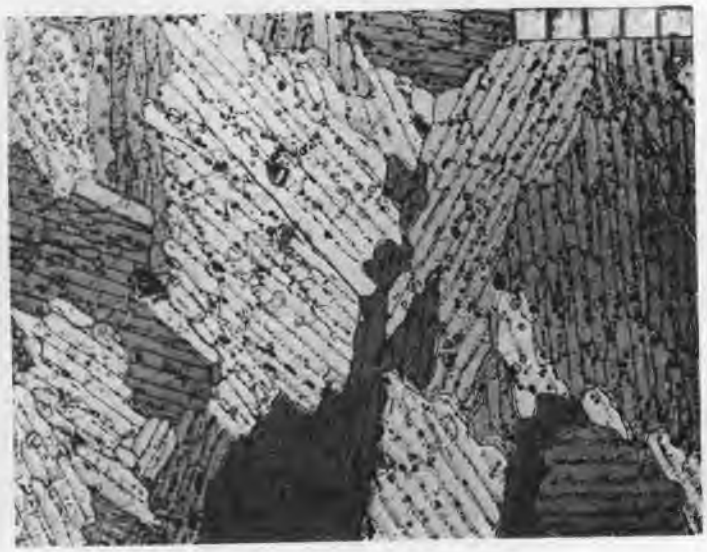

8 cm

a. Before thermal modification.

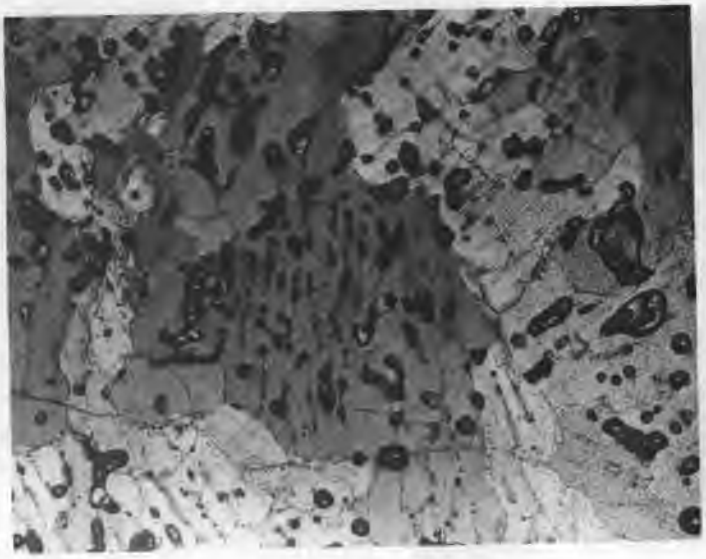

8 cm

b. After thermal modification.

Figure 11. Magnified sections of ice from slab 85-1. Scale subdivisions are 1 mm.

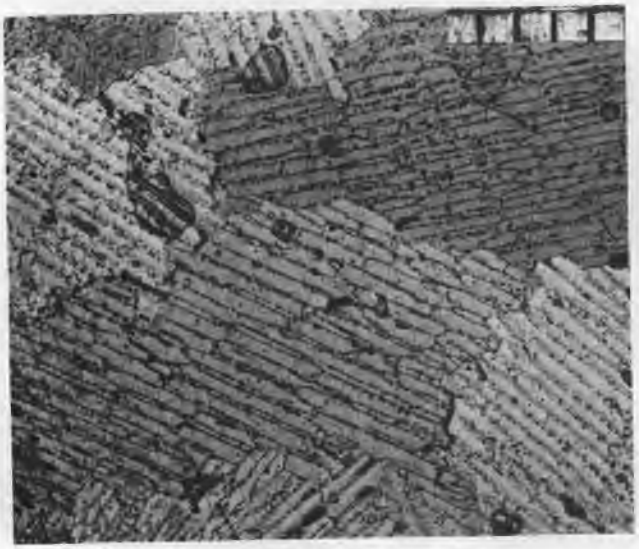

8 cm

a. Before thermal modification.

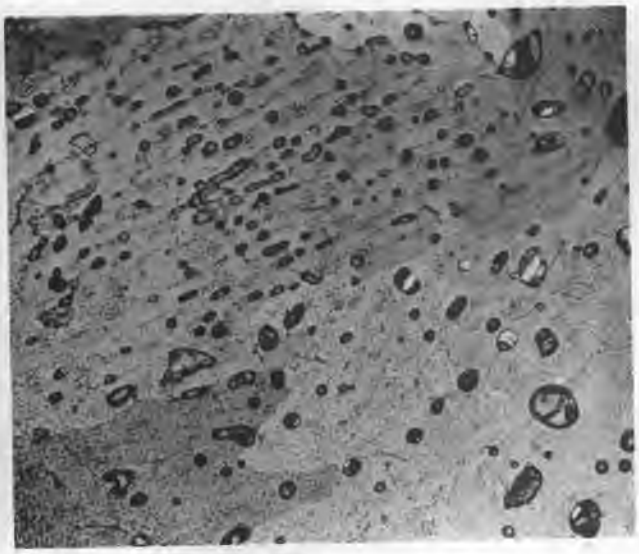

8 cm

b. After thermal modification.

Figure 12. Magnified sections of ice from slab 85-2. Scale subdivisions are 1 mm.

fresh untested ice has disappeared from the crystals of thermally modified ice. These changes are especially well documented in the enlarged structure photographs (Fig. 11 and 12) in which the original strings of brine pockets are now replaced by large bubble-like inclusions. Thermal treatment has also affected crystal outlines, which have become rounded in the thermally modified ice.

A reduction of approximately 20% in salinity measured at the end of testing clearly implies significant drainage of brine from both 85-1 and 85-2. If considered in conjunction with density measurements, this loss of brine is calculated to represent an increase of about 5% in the porosity of both slabs. As indicated earlier, in regard to the 1983–84 experiments, actual loss of brine from the slabs mainly occurs after temperatures have reached –5 °C, prior to which the actual volume of brine significantly increased because of eutectic melting of the ice by concentrated brine.

Slabs 85-3 and 85-4 were both harvested from an ice sheet that was seeded on 16 January 1985.

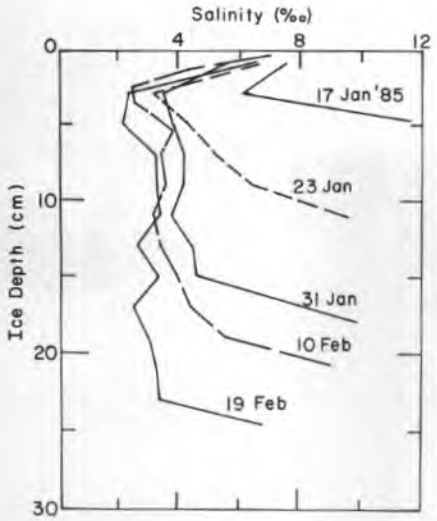

Figure 13. Salinity profiles at different stages of growth of ice sheet from which slabs 85-3 and 85-4 were harvested.

This ice sheet was regularly monitored for salinity and structure until 19 March 1985. In Figure 13 are profiles measured several days before and just after harvesting sample 85-3 on 22 January and just prior to removing sample 85-4 on 20 February. Immediately before testing, the bulk salinity of 85-3 measured 5.4‰ and that of 85-4 measured 2.4‰. By the end of testing, salinities had changed to 4.2‰ and 2.3‰ respectively. This change amounted to a 20% loss of brine from 85-3 but represented no significant drainage of brine whatsoever from 85-4. Whereas 85-3 was taken from a relatively thin (12-cm) brine-rich ice sheet (6.2‰ salinity on 23 January) the ice sheet as it existed on 20 February (now 24–25 cm thick) had begun to desalinate from the effects of rain that fell on 12 and 13 February. This resulted in some pooling of water on top of the ice but the water was pumped off before it could freeze. A light snowfall subsequently led to upward migration of brine that caused enhanced salinities in the top 2 cm of the ice sheet, as demonstrated in the 19 February salinity profile. However, enhanced salinity at the bottom of the ice sheet (evidence of recent ice growth), together with salt enrichment in the top 2 cm, was enough to raise the bulk salinity to 3.3‰. By the time 85-4 was readied for laboratory testing in July, its salinity had decreased to 2.4‰ mainly because of unavoidable drainage of brine during harvesting of the sample.

Apart from the slightly coarser grained nature of its crystals, the ice in 85-3 (Fig. 14) is structural-

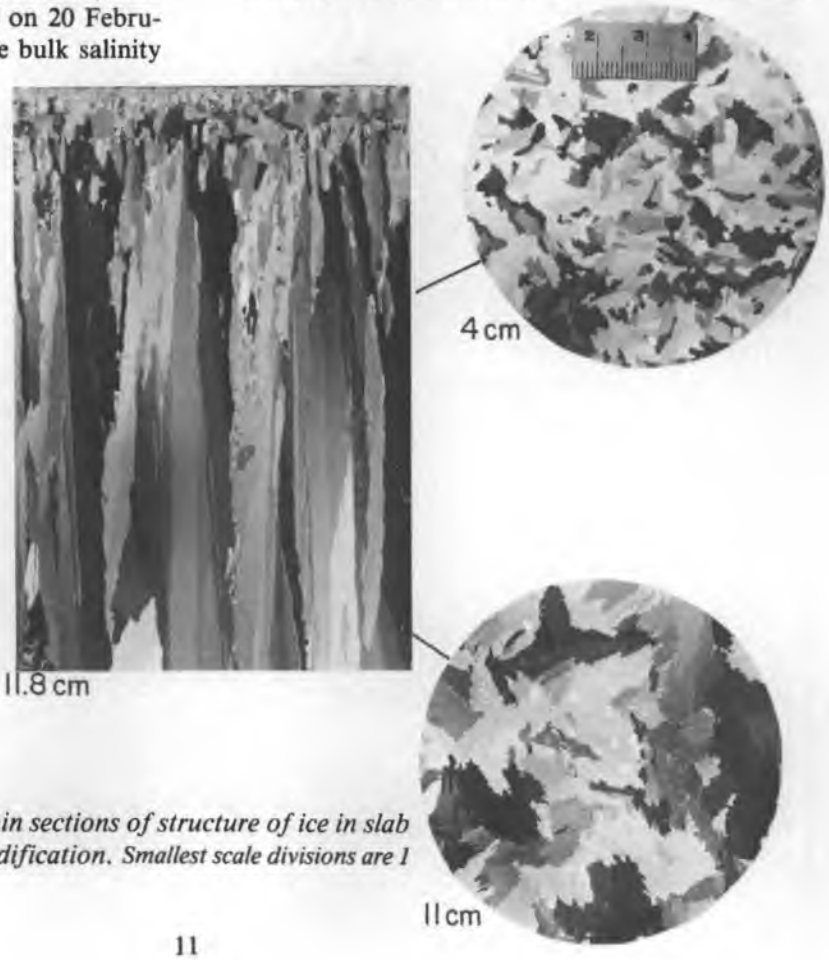

Figure 14. Vertical and horizontal thin sections of structure of ice in slab 85-3 prior to testing and thermal modification. Smallest scale divisions are 1 mm.

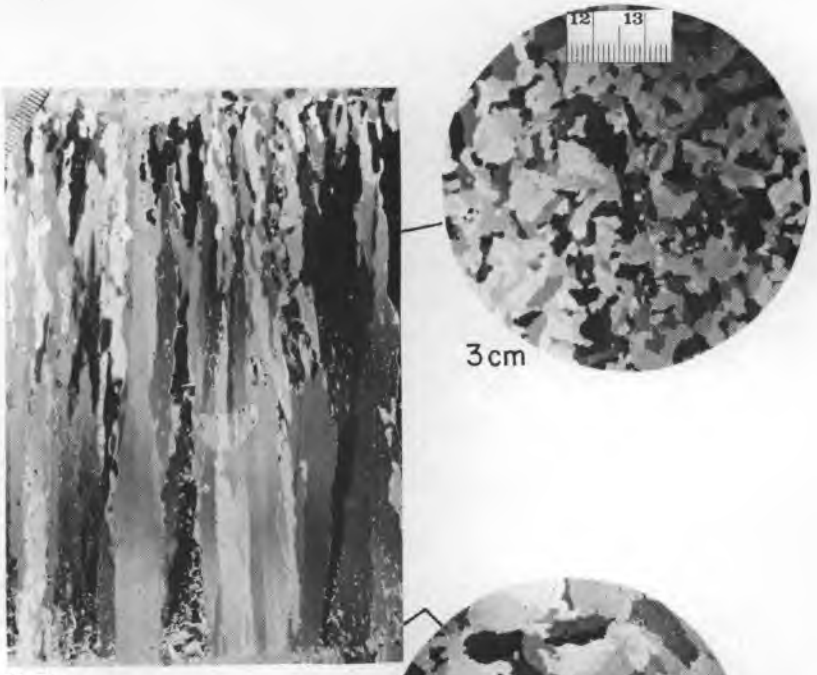

Figure 15. Vertical and horizontal thin sections of structure of ice in slab 85-3 after testing and thermal modification. Smallest scale subdivisions are 1 mm.

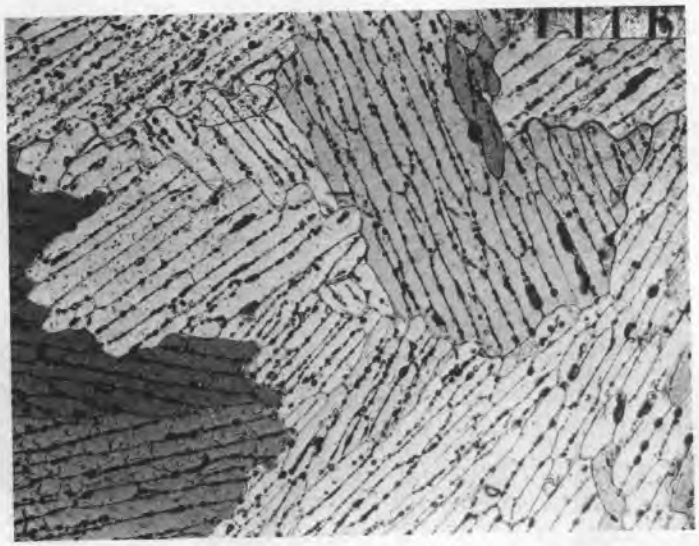

a. Before thermal modification.

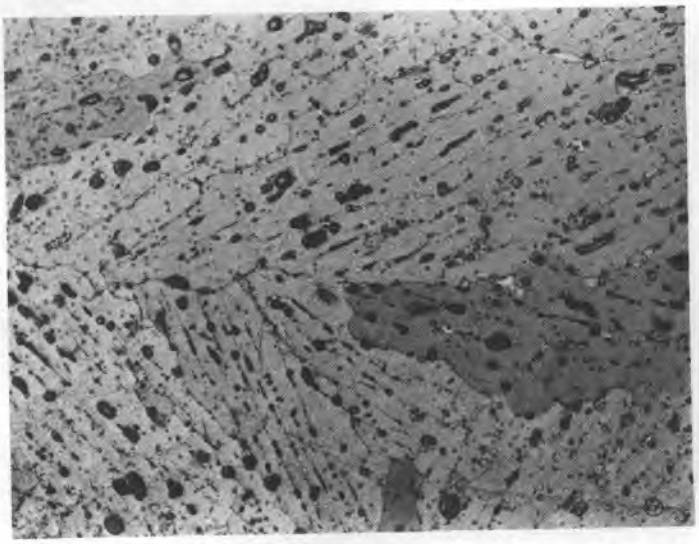

b. After thermal modification.

Figure 16. Magnified sections of ice from slab 85-3. Scale subdivisions are 1 mm.

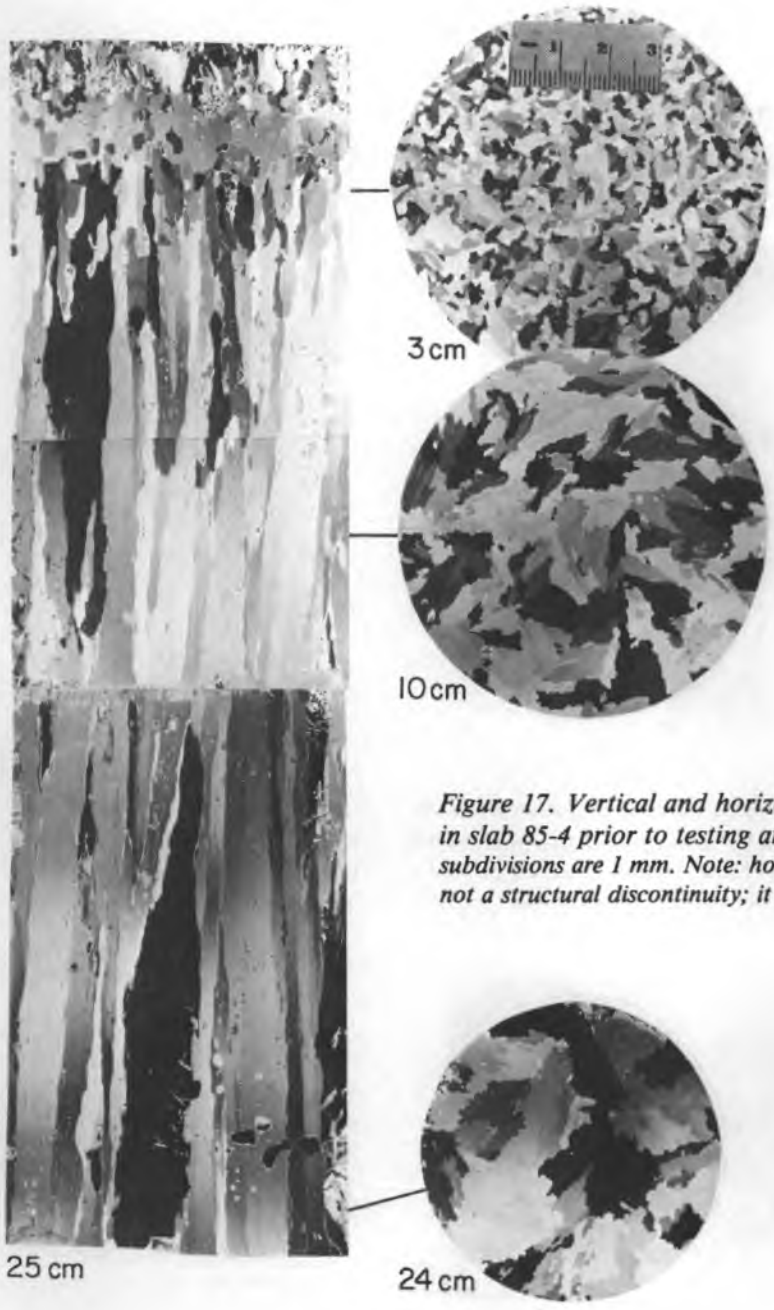

Figure 17. Vertical and horizontal thin sections of structure of ice in slab 85-4 prior to testing and thermal modification. Smaller scale subdivisions are 1 mm. Note: horizontal line at 14 cm in vertical section is not a structural discontinuity; it marks the joining of two photographs.

ly identical to that of 85-1. Structure in the thermally modified ice (Fig. 15) is also very similar to that found in 85-1 following thermal treatment, except that the original substructure of crystals in 85-3 is somewhat better preserved than in 85-1, which also contained much larger residual inclusions. Enlarged structure sections (Fig.16) indicate the extent of brine pocket modification following testing and thermal treatment of slab 85-3.

Ice in slab 85-4 shows very little difference in structure before or after thermal modification (see Fig. 17 and 18). This is in accord with the naturally degraded state of the ice sheet prior to sampling 85-4 on 20 February. In contrast to that of 85-3 the dielectric response of 85-4 was also very much suppressed, a situation entirely compatible with its low salinity characteristics.

Explanations presented by Arcone and McGrew (Part II, this report) to account for the observed change in the dielectric behavior of the 1984–85 saline ice slabs as they undergo warming from -30 °C to -2 °C are entirely consistent with the picture of temperature-controlled brine structure changes reported here.

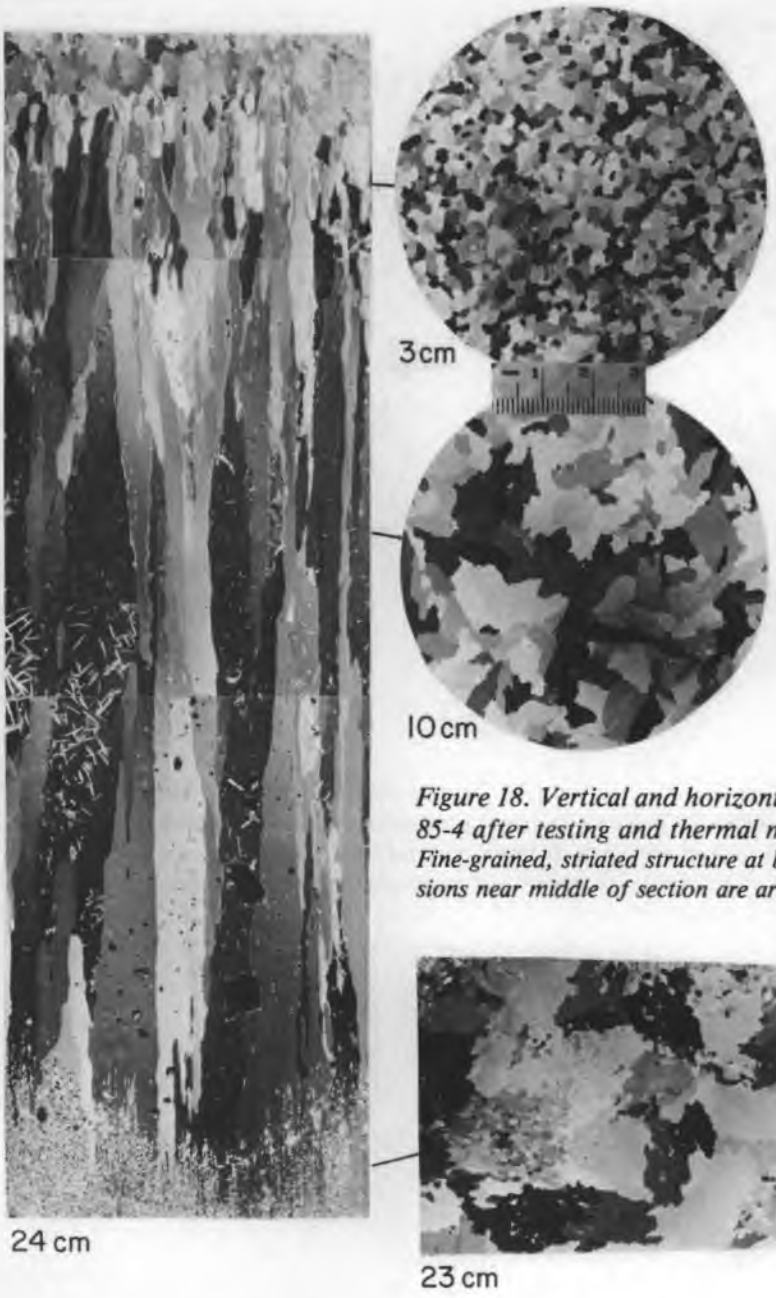

Figure 18. Vertical and horizontal thin section of structure of ice in slab 85-4 after testing and thermal modification. Scale subdivisions are 1 mm. Fine-grained, striated structure at base of vertical section and needlelike inclusions near middle of section are artifacts of thin-sectioning process.

CONCLUSIONS AND RECOMMENDATIONS

Microwave transmission measurements clearly show that the dielectric behavior of saline ice is dominated by thermally activated changes in the brine component and that changes in relative permittivity, for example, are closely related to brine volume changes but are essentially independent of the ice component. This situation arises by virtue of the freezing characteristics of salt water that produce ice composed of columnar crystals in which the brine is concentrated in vertical layers (or sheets of inclusions) sandwiched between plates of essentially pure ice. The activity of the brine is linked closely to its very sensitive response to changes in temperature, with even small changes resulting in significant changes in the size and shape of the brine inclusions. These changes in turn control the mobility and pattern of migration of brine through the ice matrix, the crystallinity of which remains essentially unchanged. The vertically elongated texture of congelation crystals in saline ice (as in natural sea ice) ensures that brine movement is also dominated by gravity-driven migration in the vertical dimension.

The need for detailed measurements of brine inclusion geometry and distribution cannot be overstressed. This has been partly addressed in measurements made here on thin sections of saline ice slabs from the CRREL pool. These measurements indicate that the shapes of brine pockets are substantially ellipsoidal, but that their sizes can vary greatly, even in the different layers of brine within a single crystal.

Any further evaluation of dielectric properties by techniques described here should include more frequent measurements of density which, in conjunction with salinity and temperature measurements, would allow more precise determination of porosity at all stages of thermal modification. Similarly, additional thin sectioning in both the vertical and horizontal dimensions would allow for more accurate assessment of changes in the sizes and shapes of brine pockets as they respond to temperature changes in the ice. To assess the dielectric behavior of new or young sea ice it would be very useful to harvest slabs under conditions cold enough to minimize brine drainage and ensure bulk salinities of 6 to 7‰ at the outset of testing.

Part II—Microwave Properties

INTRODUCTION

The dielectric properties of sea ice determine its emissivity and hence strongly influence the brightness temperature. A program has been instituted to measure microwave emission and radar backscatter of artificially grown saline ice sheets. It has been CRREL's responsibility to measure the dielectric properties of these sheets at several appropriate frequencies and to document the physical properties and ice structure as a function of the growth and decay of the ice.

Dielectric properties of sea and saline ice samples and natural sheets have been measured at discrete frequencies between 0.1 and 40 GHz, but the literature is not extensive. Hallikainen (1980) has made measurements at 600 and 900 MHz as a function of temperature, as has Addison (1969, 1970) at 100 MHz and less. Bogorodsky (1979) and Morey et al. (1984) have used pulse methods and give frequency ranges in which their results might apply. Vant et al. (1978) have measured dielectric properties as a function of frequency for a variety of conditions. All of this work shows that below about -2 °C, at brine volumes of less than about 100‰, the real part (or "dielectric constant") ϵ_r' of the complex relative permittivity ϵ_r^* generally varies from between 4.0 and 5.0 near 100 MHz to between 3.0 and 3.5 above 1 GHz, while the imaginary part (or "dielectric loss") ϵ_r'' is dominated by conductive or dispersive processes below 10 GHz. The change in ϵ_r' with frequency is most likely ascribable to a Maxwell-Wagner-Sillars type dispersion (Sillars 1937) as discussed by Addison (1970). In none of the above-referenced work was the structural condition of the ice presented.

Our objective was to measure, in the laboratory, ϵ_r^* of slab ice samples at frequencies appropriate to the concurrent radiometric and backscatter experiments, and to evaluate these data in terms of the salinity and structural characteristics of the ice slabs as they were progressively warmed from about -32 °C to -2 °C. Several sheets were grown each year and seven different slabs were removed to obtain measurements under a variety of physical conditions. The growth history in terms of thickness, temperature and salinity was recorded for each ice sheet (Part I). Once removed, the slabs were immediately brought into a coldroom to minimize brine drainage. A comparison then of the phase and amplitude of waves transmitted through the slabs gave the forward transmission coefficient from which ϵ_r^* could be calculated. Additionally, in-situ measurements of transmission attenuation using antennas above and beneath the ice sheets were made to obtain data for very young, brine-rich ice. The data were then compared with models based on data from ice thin sections and a dielectric mixing theory. This work is a continuation of results previously presented by Arcone and Gow (1985) and Gow (1985).

MEASUREMENT TECHNIQUES

A microwave bridge was used in a coldroom for these measurements (Fig. 19a). The coldroom temperature was generally held to within ±0.1 °C

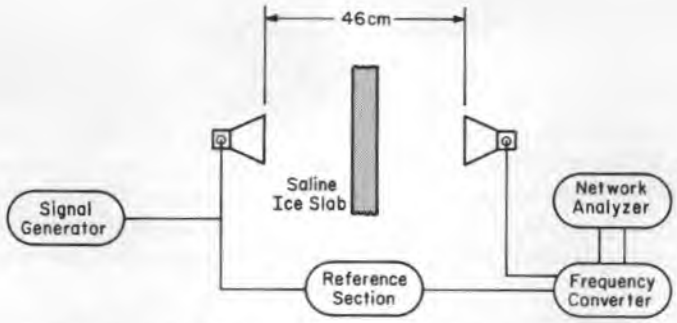

a. Schematic of microwave bridge with sample in place.

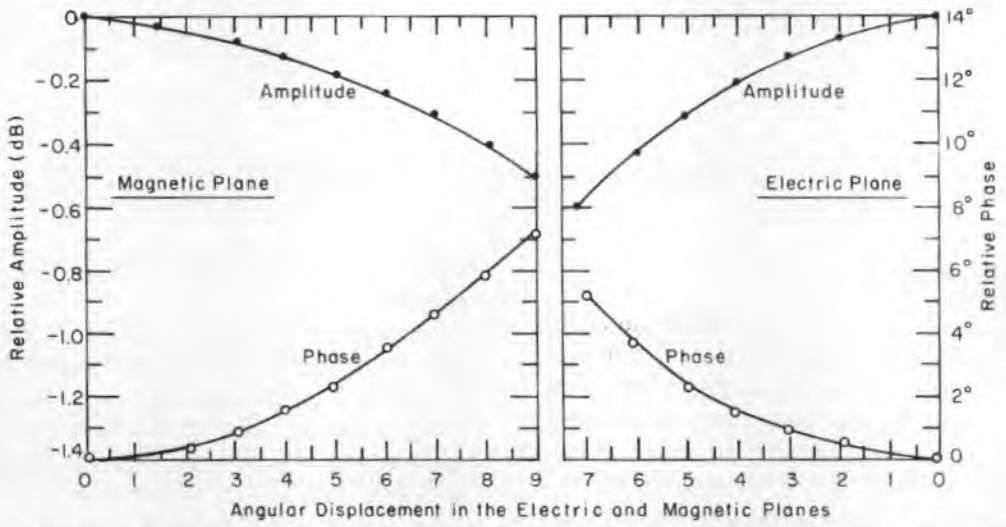

b. Distributions of amplitude and phase in the principal antenna planes across a planar interface at 11 cm from the transmit horn.

Figure 19. Schematic and field patterns of slab transmission measurement apparatus.

of the reported measurement temperature during testing for any one slab. Measurements were made approximately every three days during both warming and cooling cycles to allow the slabs to reach equilibrium. One arm of the bridge contained a reference section of coaxial waveguide while the other arm contained two opposing radiators, which were either 4.8- × 2.2-cm open-end waveguides (4.75 and 4.80 GHz) or 8.6- × 6.4-cm standard gain horns (9.50 GHz) between which the slabs were placed. The signals from both arms were then stepped down in frequency and fed into a network analyzer (Hewlett Packard Model 8410A) from which the relative phase and gain of the test arm could be read. The reading accuracies were 1 ° of phase and 0.1 dB of gain. Each radiator could rotate on its axis to allow polarization changes, and a microwave absorber surrounded all support structures to reduce unwanted reflections. The slabs themselves, approximately 46 cm square, stood vertically during testing and rested on a sliding cart to facilitate removal for an air reference measurement. The slabs were stored horizontally to permit proper brine drainage when it occurred during warming.

The distance between transmit and receive antennas was determined by the need to utilize plane wave formulations for transmission coefficients to interpret ϵ_r^* from phase and amplitude measurements, the available power in the system, and the maximum size of the slabs that could be removed from the ice sheet. A separation of 46 cm placed both receive antennas, the open-end waveguide and standard-gain horn, in the plane wave zone (i.e. the "far field" where the plane wave criteria of uniform phase and amplitude over the receive aperture is satisfied) of the transmit antennas. This separation allowed capture of the 10-dB beamwidths by the 46-cm-square slabs to minimize edge effects, and permitted a suitable signal

level for even the most lossy situation (at the warmest temperatures for the thickest slab at 24 cm), considering the low power (< 100 mW) available in our system.

Of equal importance to the use of plane wave formulation was for the slabs themselves to be in the plane wave zone of the antennas. The standard mathematical criterion for the far field is $2D^2/\lambda_0$ (D = maximum antenna aperture dimension, λ_0 is free space wavelength) which is about 7 and 46 cm for the 4.8- and 9.5-GHz systems respectively. This criterion is not satisfied by the 9.5-GHz system where a slab thickness of 24 cm would place a slab face at only 11 cm from either antenna. However, a physical optics calculation, whereby the antenna aperture was divided into an array of point dipole sources subject to the appropriate horn phase and rectangular waveguide TE_{10} mode field strength distributions (e.g. Collin 1960), revealed that 3-dB beamwidths of about 54° and 32° had already formed by 11 cm in both the magnetic and electric field planes, respectively. At this distance, within the angles of ±6° that extend from the axis of the transmit antenna to the widest dimensions of the receiver, both antennas perform as point sources producing a nearly uniform distribution of phase and amplitude over a slab face (Fig. 19b), thus justifiying the use of the plane wave formulation of the forward transmission coefficient subject to an amplitude correction (discussed below) to account for refraction collimation of the slightly diverging rays within the slab.

Phase and amplitude were recorded as a function of temperature and then compared to give the forward transmission coefficient S_{12}, the complex ratio of measured electric field strength with the slab to that measured without the slab (i.e. the air reference). This quantity was then used in the equation

$$S_{12} = W_0 W_1 (1-R^2)/(1-R^2 W_1) \qquad (1)$$

to solve for ϵ_r^* such that

$$\epsilon_r^* = \epsilon_r' - i\epsilon_r'' \qquad (2)$$

by iteration on a computer. In eq 1

$W_0 = \exp(ik_0 d)$

$W_1 = \exp(ik_1 d)$

$k_0 = 2\pi/\lambda_0$

$k_1 = k_0 n^*$

n^* = complex index of refraction = $n' - in''$

$i = \sqrt{-1}$

$R = (n^*-1)/(n^*+1)$

d = slab thickness.

The data from six different polarization positions were averaged for each temperature, as we did not expect any anisotropy due to the random orientation of dendritic planes seen between crystals. The air references for phase and amplitude were established for each polarization at each temperature. The slab faces were kept normal to the transmission axis to within 1°, as was the plane of rotation of the radiators.

The quantity ϵ_r' was determined mainly by phase, for which the reading accuracy of ±1° gave a value that was good to ±0.01. The phase readings are extremely stable, theoretically, for the slab thicknesses used, varying no more than 1° for $0.0 < \epsilon_r' < 0.5$. The quantity ϵ_r'' depended strongly on attenuation for which the reading accuracy of ±0.1 dB gave a value that was generally good to ±0.003. These sensitivities vary slightly over a 360° cycle of phase and depend also on slab thickness. The largest measured amplitude decrease from the air reference for any one slab was −15.1 dB, at an absolute level well above the noise range of the detector.

The large ratios of d/λ_0 allowed a multiplicity of solutions, generally separated by 0.6 to 1.0 for ϵ_r'. We chose those that tracked nearest 3.2 at temperatures below −26 °C, when brine volume was minimal (< 7‰) so that ϵ_r' was expected to be nearly that of freshwater ice. The separate contributions of dipolar processes and bulk conductivity to ϵ_r' could not be distinguished by only phase and amplitude measurements at one or two frequencies.

A gain was generally measured at the lowest temperatures where attenuation from propagation loss should be minimal because of the minimal amount of brine in the slabs. This gain was caused by the collimating action (dielectric focusing) of the ice whereby the divergence of the radiation is decreased when refracting through the slabs. Consequently, corrections based on a simplified, geometric optics analysis of 0.73 dB (0.73–0.87 for the thinnest slab) to 2.50 dB (2.26–2.50 for the

thickest) were subtracted from all attenuation readings. This was a significant correction at temperatures below -6 °C where average attenuation readings of less than -7 dB were generally recorded.

The geometric optics calculation assumed the transmitting antennas to be point sources from which rays diverged and were then captured by the receiving antennas, with and without the slabs present. The gain was calculated from the areal concentration of these rays after refraction through the slabs. For example, the theoretical gain caused by a 20.8-cm slab is 1.9 dB at $\epsilon_r' = 3.1$ and 2.2 dB at $\epsilon_r' = 4.0$. A 15.8-cm slab will give 1.4 to 1.7 dB of gain over the same range of ϵ_r'. These calculations apply to a ray bundle confined to less than 7° divergence from the waveguide axis, in keeping with the point source approximation. Since each collimating correction depended on ϵ_r', the solutions had to be recalculated once an approximate value of ϵ_r' was computed from the raw data. That a gain was measured at the lowest temperatures at values commensurate with the geometric optics prediction implies that the actual volume of ice studied was extremely small; probably no larger than 20 cm² in cross section for the thinnest slabs that were at the greatest distance from the antennas.

The minimum slab thickness removed was 8.5 cm, as the intrinsic strength of the saline ice precluded the taking of thinner samples. Consequently, a simple microwave transmission tester was also constructed (Fig. 20) for making in-situ attenuation readings. A slot was cut in the ice and the transmit antenna, either an open-ended waveguide (4.5–5.0 GHz), or a horn (9–10 GHz), was butted against the ice bottom. The receive antenna was then located above the ice at a height that depended on the ice thickness. The butting of the immersed antenna violated the plane wave assumption for the incident wave that was needed to interpret the data using eq 1. Therefore, we relied on the change of signal amplitude relative to an air path, with corrections made for the vltage standing wave ratio (VSWR) of the submerged horn, and an estimated relfection loss at the air/ice interface (which was minimal) to calculate an effective attenuation rate.

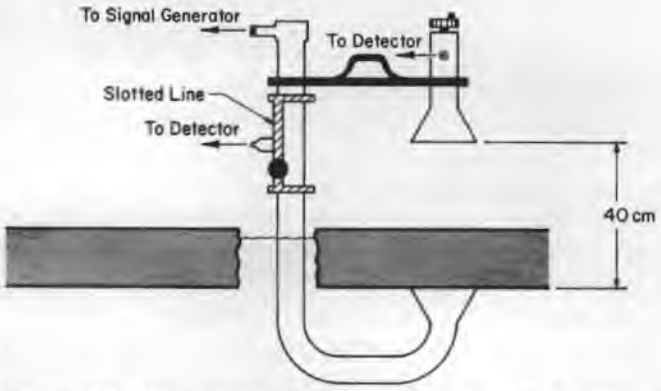

Figure 20. Microwave attenuation instrument for measuring in-situ attenuation. The slotted line measures reflection loss of the submerged transmit antenna.

RESULTS

Table 1 lists information pertinent to each slab. Most of the slabs were obtained from seeded sheets. Slabs 84-3 and 4 were removed at the same time, about 24 hours after the start of a strong warming period in the weather. Slabs 85-1 and 2 were also taken at the same time. All slabs were removed during growth and prior to any surface melting except 85-4, which was cut from the ice sheet after it had experienced one short period of flushing of fresh water from snowmelt runoff. More complete documentation of growth and

Table 1. Test slab data.

Slab	*Thickness (cm)*	*In situ* S (‰)	S *before testing*	S *after testing*	*Final density (g/cm³)*	*Seeded?*
84-2	15.3	5.0	4.4	4.0	0.883	no
84-3	20.8	5.3	3.8	3.3	0.884*	yes
84-4	20.8	5.3	3.8	3.2	0.886	yes
85-1	8.5	8.4	4.8	3.1	0.865	yes
85-2	8.5	8.4	5.5	4.4	0.885	no
85-3	11.8	6.2	5.4	4.2	0.866	yes
85-4	24.0	3.0	2.4	2.3	0.903	yes

* As measured in neighboring samples.

structural properties of the several ice sheets is given in Part I.

All slabs lost brine when they were removed from the ice sheet, and they continued to drain in the coldroom until their temperature T dropped below -24 °C. Brine drainage resumed at between -6 ° and -5 °C during testing. Each slab was melted at the end of testing and all the brine that had drained from it during testing was added to the meltwater to determine the salinity S of the slabs just before testing. The in-situ values of S in Table 1 are those for other slabs removed and immediately sampled for salinity profile measurements at the same time the slabs for dielectric measurements were being taken from the ice sheet. Calculations of brine volume v_B were made using the equations of Frankenstein and Garner (1967) or the tables of Assur (1960) based on T and S. A linear extrapolation was made between the initial and final values of S to calculate v_B after brine drainage began during warming. The values of v_B are given in the figures later in parts per thousand (‰) which may be converted to volumetric brine content by multiplying the values by 0.001.

1983–84 experiments (4.75 GHz)

The average measured values of ϵ_r' and ϵ_r'' for 1983–84 are plotted as a function of temperature in Figure 21. The vertical lines indicate the measured range as polarization was rotated. The values within each range did not vary systematically for each temperature as polarization was changed. Slab and antenna alignment were maintained for each polarization measurement. The slab faces were flat to within 1 mm although etched on the bottom side. However, the actual portion of the slabs being measured is estimated at 20 cm² or less and the accuracy of laterally repositioning the slabs between each polarization/air reference was no better than ±2.5 cm. Therefore, many different crystal groups could have been sampled during one polarization scan and this can well account for the variations seen.

The largest range in Figure 21 for ϵ_r' is only ±3% for slab 84-3 at -2.5 °C. The lowest values of ϵ_r'' occur below -22 °C and are associated with the freezing of almost all brine. The ϵ_r' values for slabs 84-3 and -4 are similar and slightly lower than those of slab 84-2 because they both lost more brine (see Table 1) in going from the pond to the coldroom and during warming. Both ϵ_r' and ϵ_r'' show little change until about -8 °C where v_B starts to increase more rapidly with warming because of eutectic melting of the ice around the brine pockets. This melting in turn leads to progressive enlargement of the pockets which begin to coalesce at temperatures of around -5 °C, ultimately forming drainage tubules near the melting point. Modeling studies, presented later, will show that this mobilization, increase in volume of brine and partial drainage of brine near the melting point are consistent with the observed dielectric behavior.

Figure 22 replots the components of ϵ_r' as a function of v_B. The quantity ϵ_r' shows a linear dependence until about a v_B value of 50‰, after which the values do not rise as steeply but show greater variance. Bogorodsky (1979) has presented a very similar curve for 100 MHz except that the dielectric values are progressively larger as v_B increases. The quantity ϵ_r'' behaves similarly but with a greater discrepancy between slabs. Although slab 84-2 consistently has the higher values of ϵ_r', it does not have consistently higher values of ϵ_r'' as might have been expected from a sample with higher salinity. Nor are the ϵ_r'' values for slabs 84-3 and -4 as similar to each other as are their ϵ_r' values. However, at the highest temperatures, slab 84-2 retained the most brine (Table 1) and produced the greatest attenuation rate (Fig. 23). The transmission attenuation β (dB/cm) shown in Figure 23 was calculated using the formula

$$\beta = 8.68(2\pi n''/\lambda_0).$$

1984–85 experiments (4.80 and 9.50 GHz)

Experimental measurements of dielectric properties of ice slabs were extended to samples taken from two of three ice sheets grown during the 1984–85 winter. Four slabs (85-1 to 4) were tested under essentially the same conditions as the 1983–84 slabs; that is, slabs were removed from the ice sheets and stored for some time at -30 °C before beginning microwave transmission measurements, which were made at regular intervals during progressive warming of the slabs from -32 ° to -2 °C. In addition, tests were repeated in reverse to evaluate the nature of the dielectric response as the slabs were cooled from -2 °C to -24 °C.

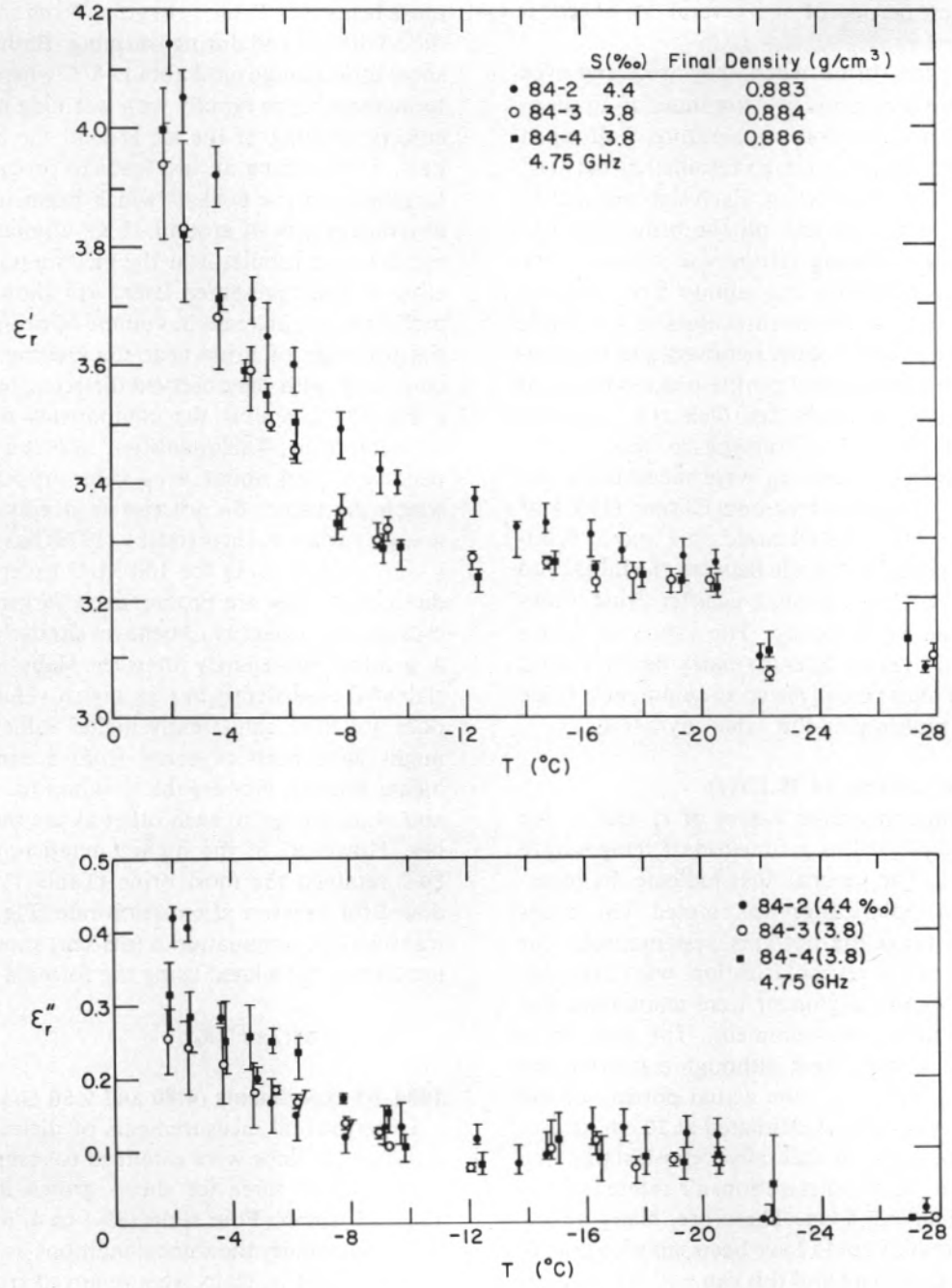

Figure 21. Relative complex permittivity vs temperature for the 1983–84 slabs.

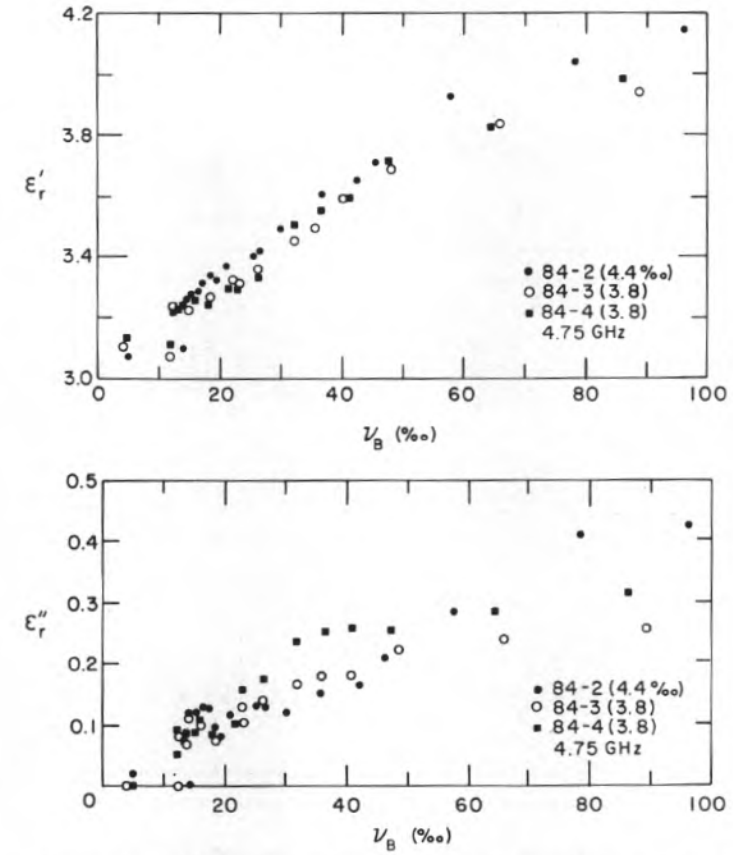

Figure 22. Relative complex permittivity vs calculated brine volume for the 1983–84 slabs.

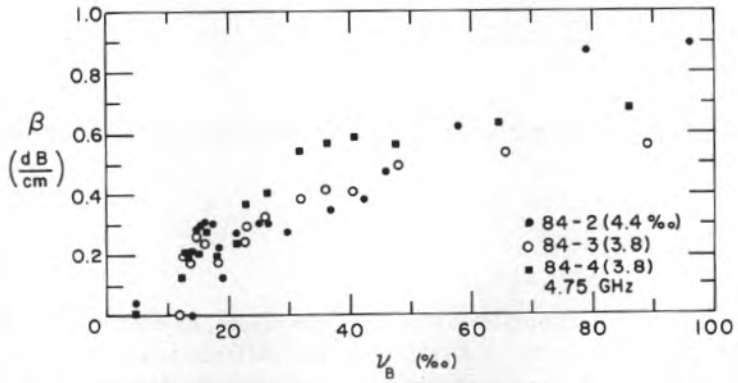

Figure 23. Transmission attenuation vs calculated brine volume for the 1983–84 slabs.

The quantity ϵ_r^* is plotted vs T for the four slabs in Figures 24 and 25 at 4.80 and 9.50 GHz, respectively. The filled circles are the initial warming cycle and the open circles are the cooling cycle. Both figures show lower values of ϵ_r' during the cooling cycle, as expected from the replacement of brine with air. The youngest slabs, 85-1 (seeded) and 85-2 (unseeded), give similar ϵ_r' values, suggesting that crystal size is not an important factor. The oldest, thickest and most desalinated slab, 85-4, shows the least separation between warming and cooling values of ϵ_r' as it had the least loss of brine. In addition the response of ϵ_r' to warming in slab 85-4 was very much suppressed with respect

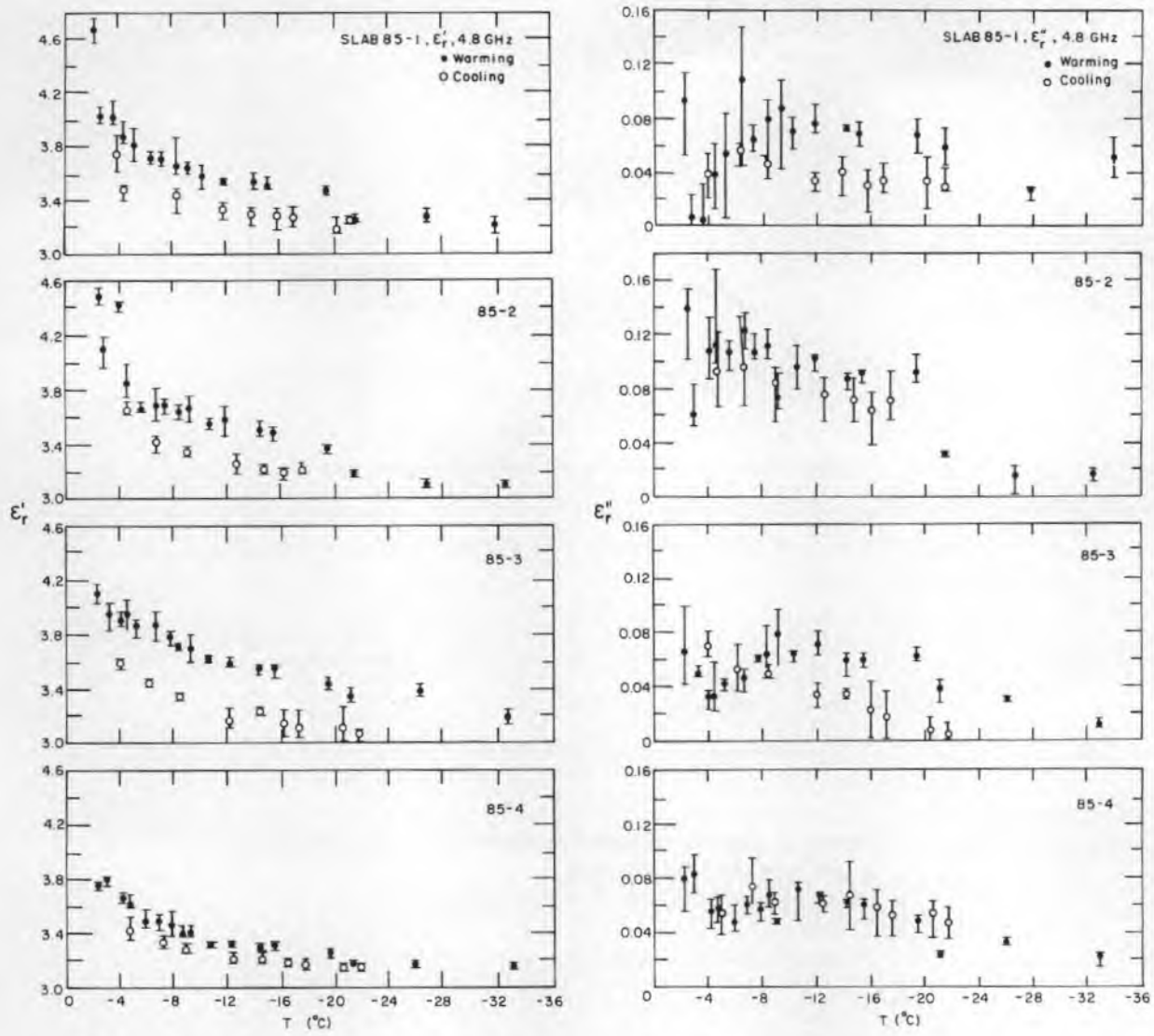

Figure 24. Relative complex permittivity vs temperature for the 1984–85 slabs, 4.80 GHz.

to all other 1985 slabs, a situation compatible with its low salinity characteristics. Some measurements, mostly for slab 85-3, show the cooling cycle values below −16 °C to be consistently below 3.18, an ϵ_r' value previously reported for pure ice at −20 °C (Glen and Paren 1975). These less-than-pure ice values are due to the presence of air pockets derived from drainage of some of the brine pockets still remaining in the original ice at these temperatures. The range of most measurements never exceeds about ±5%.

Generally slabs 85-1, 2 and 3 show the cooling cycle values of ϵ_r'' to be lower than the warming cycle values, as expected from the loss of brine, but the differentiation is not great. Although the ϵ_r' temperature dependencies compare favorably between 1983–84 and 1984–85, a similar comparison of the behavior of ϵ_r'' is distinctly different, either between any two slabs or on the average. The values never increase in the 1985 data to the range of 0.2 to 0.4 as they did in 1984. In fact, slabs 85-1 and 3 (4.80 GHz) and 85-1 and 2 (9.50 GHz) show some very low values and erratic behavior in the −6 to −2 °C range. Possible causes for the 1983–84/1984–85 differences are discussed later.

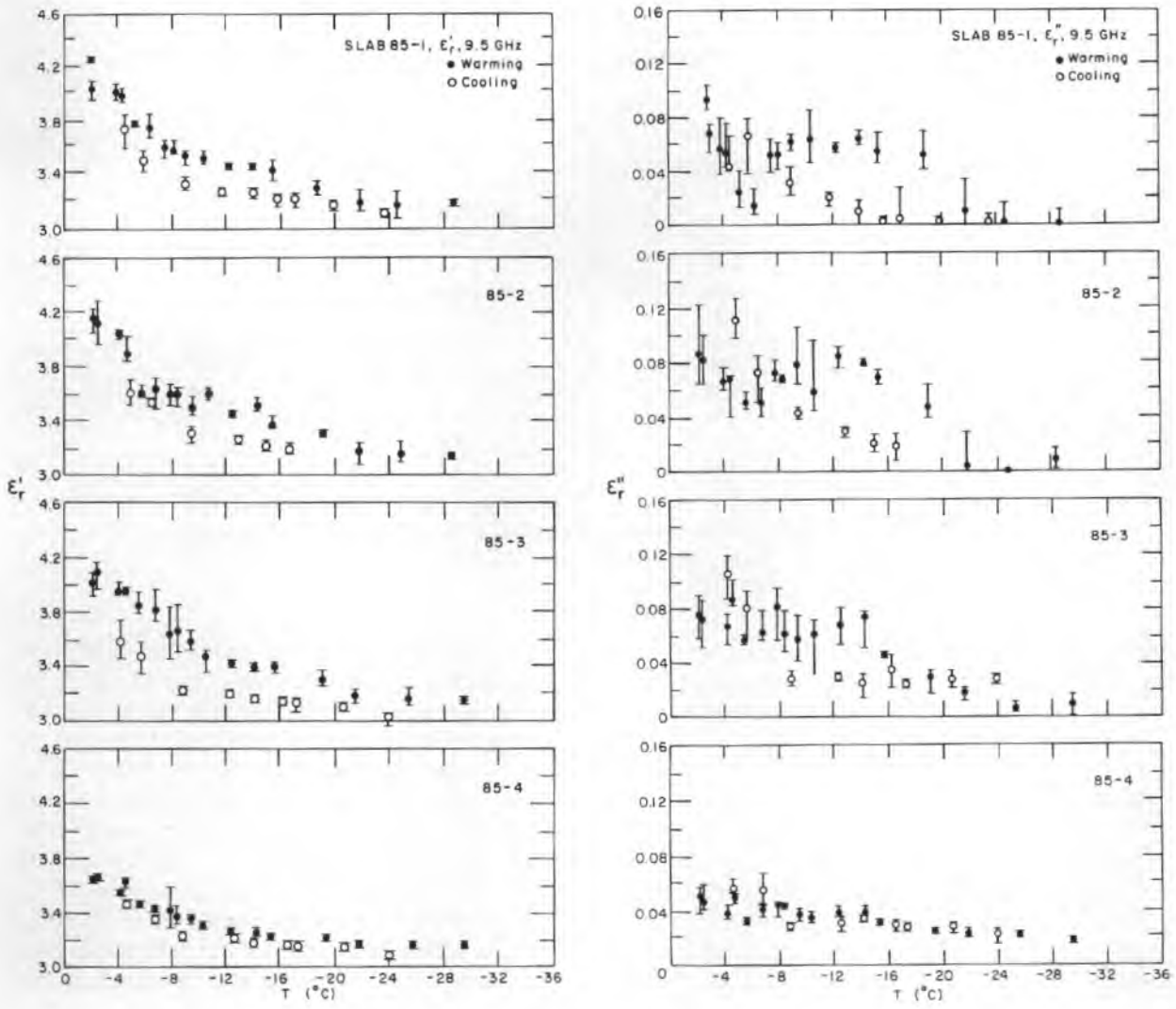

Figure 25. Relative complex permittivity vs temperature for the 1984–85 slabs, 9.50 GHz.

1984–85 in-situ experiments

Table 2 summarizes the in-situ attenuation measurements. The average salinity was that of a full thickness sample and the average temperature is the mean of the surface and bottom temperatures. The loss was measured relative to an air path whose own loss left only about a 50- to 60-dB range for measurement. A correction was made for reflection losses at the ice/submerged transmit antenna interface (measured) and at the air/ice interface (estimated). The seven measurements in Table 2 not in the noise range of the detector vary between 4.1 and 8.7 dB/cm. The highest loss rate occurred in the thinnest ice, which was also relatively warm and thus had the highest value of v_B. These calculated values of v_B are generally high and complement the range of v_B values in Figure 23. By comparison with Figure 23, Table 2 shows that the attenuation rate β will start to increase dramatically above 100‰.

The 9- to 10-GHz attenuation rate is always larger than the 4.5- to 4.8-GHz rate over the first eight values of Table 2. This contrasts with the lower brine volume data of Figures 24 and 25, which when averaged, will be shown below to give more comparable ϵ_r'' values for the two frequencies in 1984–85. Similar, high in-situ attenuation rates that increase with frequency for young ice have also been reported by Bogorodsky (1979). Attenuation rates due only to d.c. conduction currents are very similar at both frequencies (discussed later) and so cannot be responsible for this attenuation increase with increasing frequency. The dielectric mixing model discussed in the next section

Table 2. In situ loss measurements, 1985.

Sheet number	Thickness (cm)	Frequency (GHz)	Transmission loss (dB)	Loss (dB/cm)	T (°C)	S (‰)	Est v_B^* (‰)
2	7.1	4.5	41.6	5.9	-4.5	9.1	101
2	7.1	10.0	43.5	6.1	-4.5	9.1	101
2	9.1	4.8	37.5	4.1	-3.0	9.2	149
2	9.1	9.0	>52.6	>5.8	-3.0	9.2	149
3	5.8	4.8	29.6	5.1	-2.2	8.4	183
3	5.8	9.0	50.5	8.7	-2.2	8.4	183
3	6.9	4.8	36.9	5.3	-2.0†	6.7	161
3	6.9	9.15	51.8	7.5	-2.0	6.7	161
3	12.0	4.8	>52.2	>4.4	-2.9	5.8	97
3	12.0	9.0	>52.2	>4.4	-2.9	5.8	97
3	24.0	4.8	>52.2	>2.2	-1.1	3.2	146
3	24.0	8.9	>52.2	>2.2	-1.1	3.2	146

* Brine volume calculated from the equations of Frankenstein and Garner (1967) and the tables of Assur (1960) using average values of temperature and salinity.
† Surface temperature is estimated.

does predict an attenuation increase with frequency, but requires a bulk d.c. conductivity term to give the right attenuation order of magnitude.

DISCUSSION

Comparison of data

Figure 26 plots the averages of ϵ_r' based on all values occurring within increments of 5‰. Averages were taken only where at least three data points in an increment occurred. The plots show that, during both warming and cooling cycles, ϵ_r' was slightly greater at 4.80 GHz than at 9.50, which is consistent with past dispersional models of sea ice (Addison 1970, Vant et al. 1978) and the one discussed later. Figure 26 also shows other values reported at 4 and 10 GHz (Bogorodsky and Khoklov 1975, Vant et al. 1978; all values given in Vant et al. 1978) for samples for which brine volumes were calculated from the given values of T and S. There is reasonable agreement up to about 60‰ at which point many of our data points seem to merge. This is misleading, however, as our

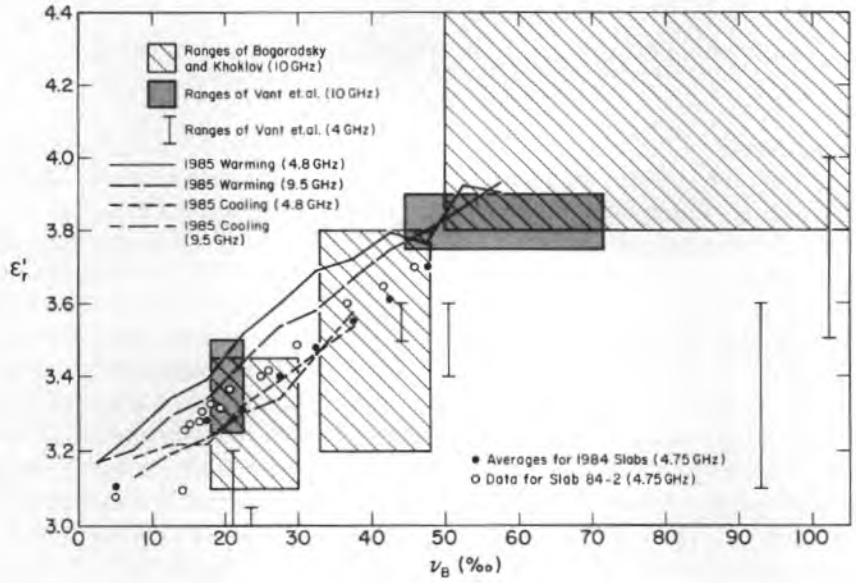

Figure 26. ϵ_r' vs v_B (‰) comparisons between data averages for 1983–84 and 1984–85 slabs, and with data of previous research for ϵ_r'.

measurements above 50‰ at 9.50 GHz varied between 3.6 and 4.3, a variation similar to that of Bogorodsky and Khoklov (1975).

Figure 26 also shows that at any one value of v_B, the 1984–85 cooling cycle value of ϵ_r' may be 2 to 8% lower than the warming cycle value. A conversion of the "before" and "after" salinities (Table 1) into brine volumes (at -2 °C) gives a maximum percentage gain in air volume of about 3 to 4% due to the drained brine. For example, the salinity changes in slab 85-3 translate to a density change during testing from 0.906 to 0.872 g/cm³ (actual final value = 0.865 g/cm³) or about 3% gain in air volume. The average observed decrease in ϵ_r' at, for example, v_B = 40‰ is 4.0% for all 1985 slabs and 4.3% for slabs 85-1, 85-2 and 85-3, which drained the most brine.

This close correlation between decrease in ϵ_r' and gain in air volume during warming suggests that modifications in the brine structure from thermal effects do not significantly affect ϵ_r'. This is consistent with the thin-section studies, which show retention of individual brine inclusions in the thermally modified ice, although without strong alignment along dendritic planes. This correlation is also consistent with the comparison of 1984 averages with those for the 1985 cooling cycles (Fig. 26) which is close because slabs 84-3 and -4 had values 5–7% lower than the 1985 slabs' warming values. These lower values of ϵ_r' could be partially caused by some loss of brine structure (i.e. discrete inclusions) due to warm weather, but more probably to a loss in brine volume. The air temperature at the time of removal of these slabs was near 7 °C (from a previous overnight low of -2.9 °C) and much brine was lost upon extraction and transport of the slabs to the coldroom. This loss of brine was estimated using the salinity data of Table 1 and used to estimate the initial densities of the slabs before dielectric testing. The values obtained were utilized for the modeling discussed in the next section.

Figure 27 compares ϵ_r'' data averages from 1983–84 and 1984–85 with ranges of values from Bogorodsky and Khoklov (1975) and Vant et al. (1978). The 1984–85 data are only for the warming

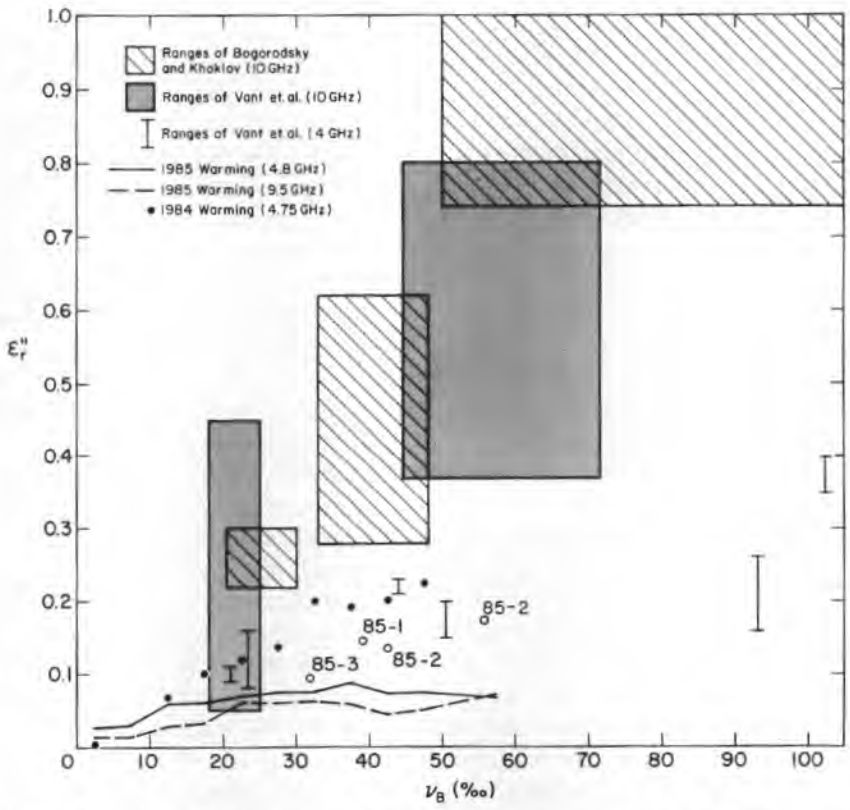

Figure 27. ϵ_r' vs v_B (‰) comparisons between data averages of 1983–84 and 1984–85 slabs and with data of previous research for ϵ_r''. Open circles are maximum values measured for indicated slabs at 4.80 GHz.

Table 3. Saline ice structural parameters.

		Brine inclusions						Dendrites			
		Average c/b axial	Max/Min[a] (mm) length	width	Average vertical length		Depth of hor. section analyzed	Section analyzed	Average[b] tilt θ	Average spacing	
Slab	Seeded?	ratio (S.D.)	b	c	(mm)	(S.D.)	(cm)	(cm)	(°)	(mm)	(S.D.)
85-3	Yes	0.427 (0.260)	0.96/0.12	0.30/0.05	0.91	(0.91)	11	2–11.8	4	0.41	(0.08)
85-3 THERM MOD		0.426 (0.220)	1.22/0.14	0.34/0.07	0.84	(0.31)	11	2–11.8	2	0.43	(0.11)
85-2	No	0.460 (0.173)	1.46/0.05	0.40/0.03	0.91	(0.43)	8	3– 8.5	12	0.39	(0.11)
85-2 THERM MOD		0.442 (0.199)	1.68/0.05	0.52/0.02	1.14	(0.51)	8	3– 8.5	13	0.43	(0.09)
84-3,4	Yes	0.417 (0.188)	0.35/0.04	0.19/0.01	0.93	(0.66)[c]	4	4–20.0	2	0.39[d]	(0.10)
84-3,4 THERM MOD		0.439 (0.197)	0.74/0.09	0.21/0.01	0.33	(0.15)[e]	3	4–20.0	3	f	

a—Range pertains only to inclusions measured in a random sampling. Actual limits slightly greater (or less for minima).
b—20 crystals surveyed.
c—Drainage structure had developed; could not trace dendrites.
d—Can change with depth.
e—Mainly small circles along vertical lines; some very large pits (3.3 mm).
f—Dendrites could not be distinguished.

cycle to facilitate the comparison. The plots show the distinction between the 1983–84 and 1984–85 slabs in v_B dependency above about 20‰. The 1983–84 data and a few isolated maximum values measured in 1984–85 are consistent with Vant et al. (1978) at 4 GHz. The 9.50-GHz values at $v_B <$ 50‰ are slightly lower than those at 4.80 GHz for the 1985 slabs; this is not consistent with the theoretical model discussed below, which predicts slightly higher values at 9.50 GHz due to the brine whose loss peaks around 9 GHz. However, the order of magnitude is consistent with the model. The agreement with Vant et al. (1978) at 10 GHz is poor, although there is some overlap. There is no overlap with the data of Bogorodsky.

Possible explanations for the difference between the 1983–84 and 1984–85 values of ϵ_r'' above brine volumes of about 20‰ were investigated but are inconclusive. The difference seems related to bulk conductivity, which is discussed later. The phase and gain meters of the network analyzer were all found to be in calibration after the 1985 testing, although we cannot discount temporary malfunctioning. (The extreme dependence of ϵ_r' upon phase precluded any possibility of an uncalibrated gain meter affecting the validity of the ϵ_r' calculations.) Structural thin sections (Table 3) examined prior to testing revealed the 1983–84 brine pockets to be vertically longer and narrower than those seen in the 1984–85 slabs, and this may be related to greater conductivity. However, these sections were taken, not from the slabs, but from adjacent samples because we did not want to disturb the slabs prior to testing. All thin sections of thermally modified ice were taken from the slabs themselves. It would have been desirable to remove additional slabs for simultaneous warming and thin sectioning to examine structural changes occurring during testing, but this was not done in order to minimize disturbing the ice sheet for other experiments.

Some general differences between the 1983–84 and 1984–85 slabs are evident. Compared with 1984, density is lower in slabs 85-1 and 3 (both of which had very low values of ϵ_r'' near -4 °C), age (or thickness) is less in slabs 85-1, 2 and 3, and the temperature of initial freezing for all sheets was much higher in 1985 (freezing was initiated at about -20 °C in 1984 but only at about -10 °C in 1985). The modeling data (below) show that the ϵ_r'' values below v_B = 60‰ can be matched for the 1984–85 slabs by assuming a brine-volume-dependent bulk conductivity that never exceeds 0.03 S/m (siemens/meter), whereas values up to 0.06 S/m are generally required for 1983–84 slabs. Therefore, a greater continuity of conductive

channels (i.e. permeability) may have existed in the 1983-84 slabs, possible due to their older condition.

Analytical modeling

Any theory of dielectric properties in the VHF through microwave range should account for 1) a decrease in ϵ_r' with increasing frequency; 2) an increase in both ϵ_r' and ϵ_r'' with increasing v_B; 3) at least two loss mechanisms, with total loss (ϵ_r'') increasing as frequency decreases into the HF range; and 4) very high microwave losses at high values of v_B, with attenuation increasing with frequency. The dielectric mixing model given in Vant et al. (1978) and discussed in the appendix meets these criteria with the following exceptions: 1) as frequency decreases toward and below 100 MHz, ϵ_r'' eventually increases—an impossibility for the known, finite values of sea ice conductivity (Thyssen et al. 1974, Timco 1979); and 2) the predicted losses at high values of v_B are not as high as observed. The error lies in the lack of an additional loss mechanism, namely bulk conductivity σ_{bulk}, which reflects the permeability of sea ice. In addition, our thin section studies reveal a much different brine inclusion geometry than was assumed and derived by Vant et al. (1978). All dielectric mixing models consider only unconnected inclusions.

The Vant et al. (1978) model assumes that the large and increasing values of ϵ_r'' that occur as frequency decreases toward 100 MHz result from an assumed angular displacement θ of 35°-45° of the long axes of ellipsoidal brine pockets from the (vertical) direction of wave propagation. The angle θ would also be the displacement of the ice crystal c-axes from horizontal. The ellipsoids are assumed to have circular cross sections (i.e. are prolate spheroids), the diameters of which are much shorter than that of the long axis so that a moderate value of θ is needed to permit strong coupling of the horizontal electric field into the brine ellipsoids. Although this model will give higher loss near 100 MHz, eventually ϵ_r'' will decrease as frequency decreases below 100 MHz, at any θ value. This decrease is not compatible with the behavior of a conductive material.

Prior to modifying this model, measurements were made on enlargements of the thin-section photographs shown in Part I. Brine pocket geometry in both the horizontal and vertical planes was examined for several slabs and the data are summarized in Table 3. Below about 6 cm in the unseeded ice and about 1 cm in the seeded ice, the dendritic planes (which are normal to the c-axes) seen in vertical thin sections show only marginal tilt θ, which average 13° or less from vertical. The horizontal thin sections show the cross sections of the brine inclusions to range from circular to elliptical (long b axes parallel to the planes, c axes perpendicular). In the horizontal plane, then, the brine pockets are generally ellipsoidal as well as being ellipsoidal in the vertical plane in which the vertical a axis is still the longest. Therefore, our ellipsoids contain three unequal axial lengths with $\theta \equiv 0°$. This ellipsoidal geometry in the horizontal plane gives the same qualitative results for ϵ_r'' as Vant et al. (1978) obtained and also predicts that ϵ_r'' must eventually decrease with decreasing frequency, at any value of θ. Therefore a conductivity loss term is still required.

The Vant et al. (1978) model is therefore modified by setting $\theta = 0°$ and adding a bulk d.c. conductivity loss term ($-i\,\sigma_{bulk}/\omega\epsilon_0$ where ω is frequency in rad/s and $\epsilon_0 = 8.85 \times 10^{-12}$ F/m). Conductivity values ranging from 0.03 to 0.003 S/m have been reported for sea ice (Thyssen et al. 1974, Timco 1979), values sufficient to produce the losses observed by Vant et al. (1978) at 100 MHz. σ_{bulk} has been measured indirectly through interpretations of Schlumberger sounding curves for ice sheets grown in 1986 (Arcone 1987). The values ranged from 0.5 ($v_B \cong 200‰$) to 0.1 ($v_B \cong 2‰$) for freshly growing ice with a great deal of variability.

Figure 28 compares the 4.80-GHz experimental data with the revised model (eq A4, Appendix A), employing the data of Table 3, depolarization coefficients for ellipsoids of three unequal axial lengths (Osborn 1945), and brine conductivity and dielectric values from Stogryn and Desargent (1985). The figures list the mean axial lengths for each slab, the ratios of which were used to compute the depolarization coefficients that are also given. The ratios of importance are b/a and c/a, which were computed from the average brine inclusion dimensions. The quantity c/b given in Table 3 is the mean of the individual ratios of the horizontal axes and not the ratio of the mean lengths.

The models give good quantitative comparisons with ϵ_r' for slabs 84-3 and 4 and for the cooling cycles of slabs 85-2 and 3. These good comparisons are for slabs that had already desalinated appreciably and, therefore, probably had weaker electrical interactions between inclusions. In all cases both theoretical and experimental warming cycle data correlate qualitatively between -6° and

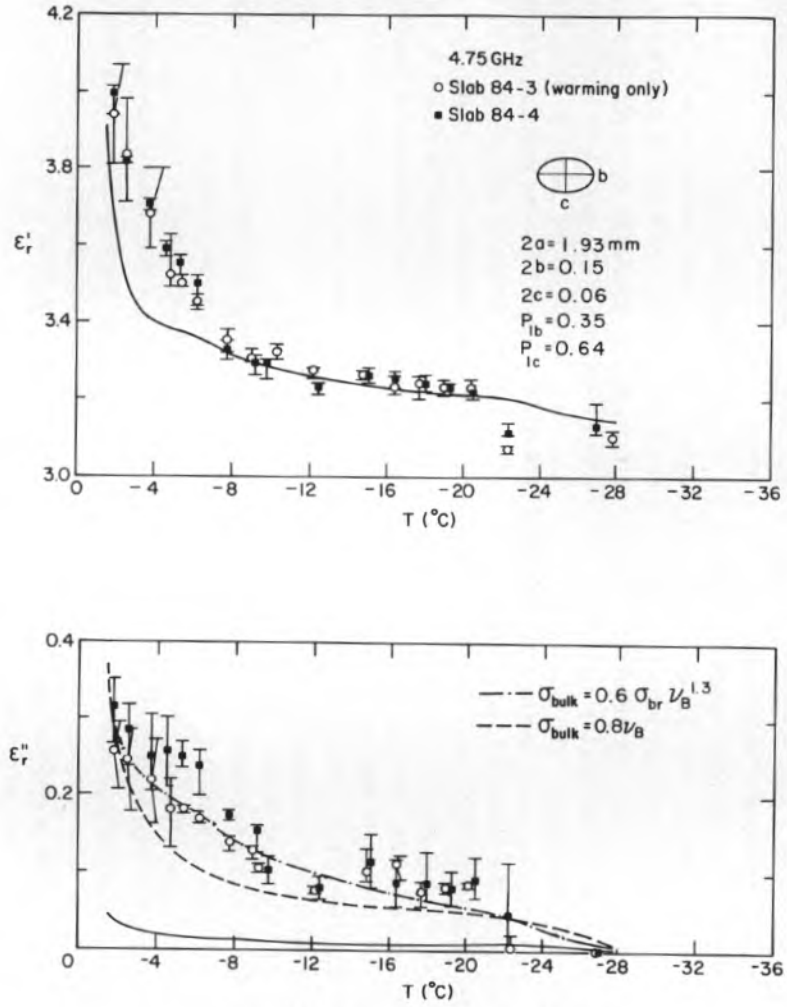

a. Data for slabs 84-3 and 84-4.

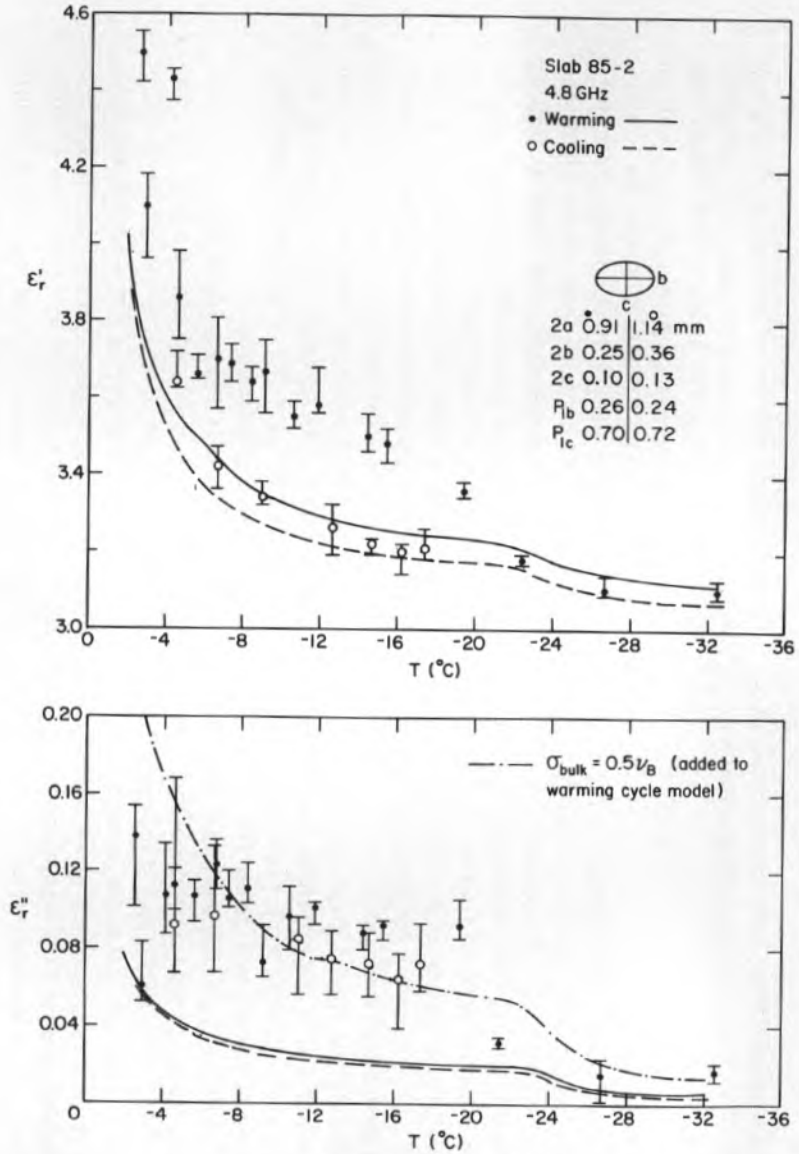

b. Data for slab 85-2.

Figure 28. Comparisons of experimental data with predictions of dielectric mixing theory presented in the Appendix. Brine dielectric parameters taken from Stogryn and Desargent (1985); brine pocket depolarization coefficients taken from the curves of Osborn (1945); brine inclusion model ellipse is in the horizontal plane with b the direction of the dendritic planes; depolarization coefficient $P_{1a} = 1-(P_{1b}+P_{1c})$*;* a, b, c *are semi-axis lengths;* σ_{br} *= brine conductivity.*

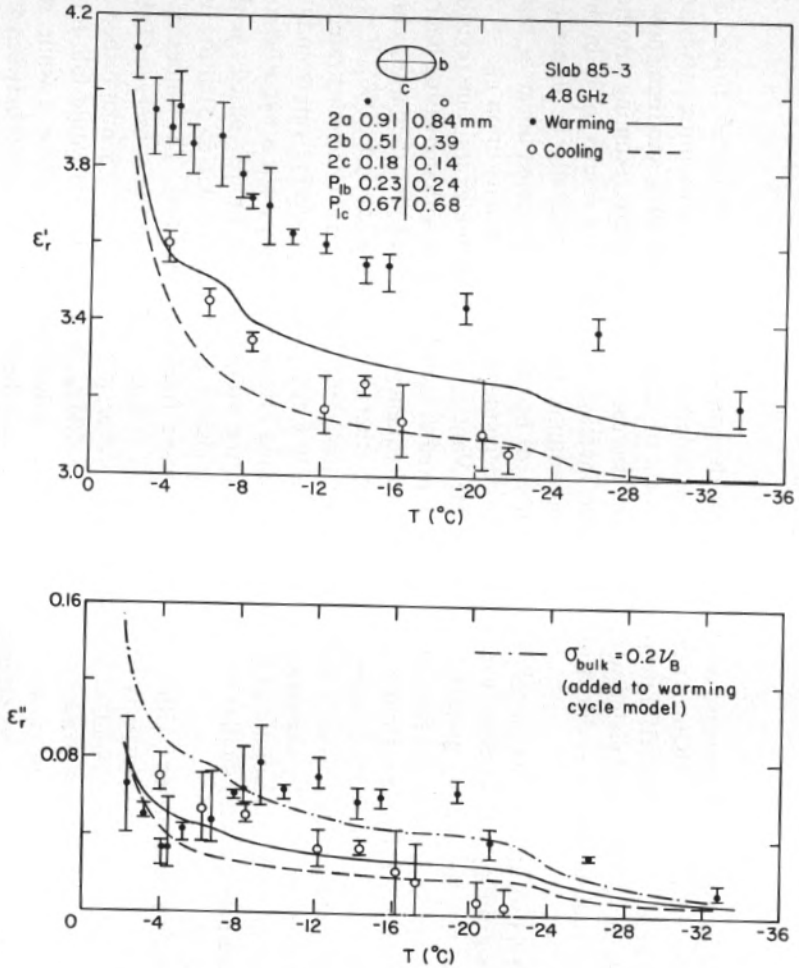

c. Data for slab 85-3.

Figure 28 (cont'd).

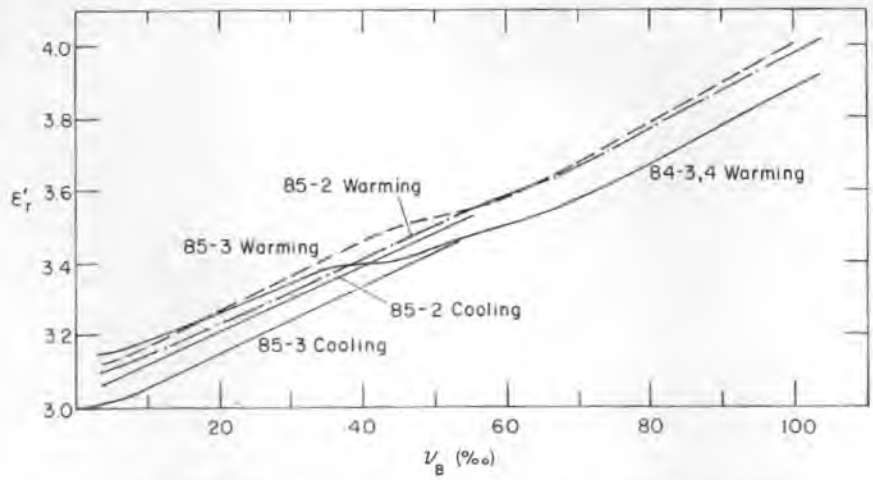

Figure 29. Model results for ϵ_r' vs brine volume at 4.80 GHz.

–8 ° and above –24 °C in the rate of decrease of ϵ_r' with decreasing temperature. The change near –8 °C results from changes in brine electrical properties and the change at –24 °C is associated with the precipitation of sodium chloride dihydride (Assur 1960).

Slab 85-3 (Fig. 28) shows greater theoretical discrepancy between warming and cooling cycles than does 85-2, reflecting the slightly greater loss in brine suffered by slab 85-3 and lower final density. Only small differences between warming and cooling cycle depolarization coefficients were calculated for each slab, eliminating this as a likely explanation for the differences. The similarity of these axial ratios and of the initial salinity of both slabs before warming produce very similar warming curves for ϵ_r'.

Improved quantitative comparisons with ϵ_r'' are achieved by adding a bulk d.c. conductivity term, except in the case of slab 85-3. Linear and/or Winsauer type exponential (Ward and Fraser 1967) empirical dependencies of σ_{bulk} upon v_B were assumed in one case as was done by Thyssen et al. (1974). These empirical conductivity terms do not explicitly state any dependency upon permeability; the dependency is implicit in the brine volume proportionality. The permeability factor is the most likely cause of differences in ϵ_r'' between the 1983–84 and the 1984–85 slabs. The lack of consistent differentiation between warming and cooling cycle experimental values in Figures 28b and 28c implies that brine volume is not as strong an influence upon dielectric contributions to ϵ_r'' as it is upon ϵ_r'.

Figure 29 replots the 4.80-GHz modeling results for ϵ_r' as a function of v_B. The cooling curves show linear dependency to 55‰, the highest brine volume attained in this cycle. The warming curves are all linear to between 40 and 60‰ and then show a slight decrease in slope before resuming another linear increase. The modeling results for ϵ_r'' in this brine volume range will naturally be linear (or nearly so) because of the assumed linear or nonlinear dependence of conductivity upon v_B.

The Vant et al. (1978) model and our revision both predict increasing loss with increasing microwave frequency, but do not give the large values we and others have observed at $v_B > 100$‰ if σ_{bulk} is not included. This low loss is demonstrated in Figure 30 which gives theoretical ϵ_r^* values and the associated attenuation rates β for a hypothetical, high brine volume sea ice model (based on the brine inclusion parameters of slab 85-3) at the two microwave frequencies studied. The values of β for $\sigma_{bulk} = 0$ are much lower than observed (Table 2). However, if $0.2 < \sigma_{bulk} < 0.5$ S/m at brine volumes > 100‰, then β (Fig. 31) would fall in the range of values observed in Table 2 while still maintaining the 2- to 4-dB difference between 4.80 and 9.50 GHz. Note that Figure 31 shows attenuation rates due only to d.c. conduction to be nearly equal at both frequencies, so that d.c. conduction cannot be responsible for an increase of attenuation with frequency. The high values of β observed in Table 2 therefore suggest that bulk conductivity does have an exponential dependency on brine volume that increasingly dominates attenuation as v_B increases above 100‰.

Although the structural and salinity characteristics of the saline sheets simulate natural conditions, removal of slabs or any other type of sample is always accompanied by brine drainage, as evi-

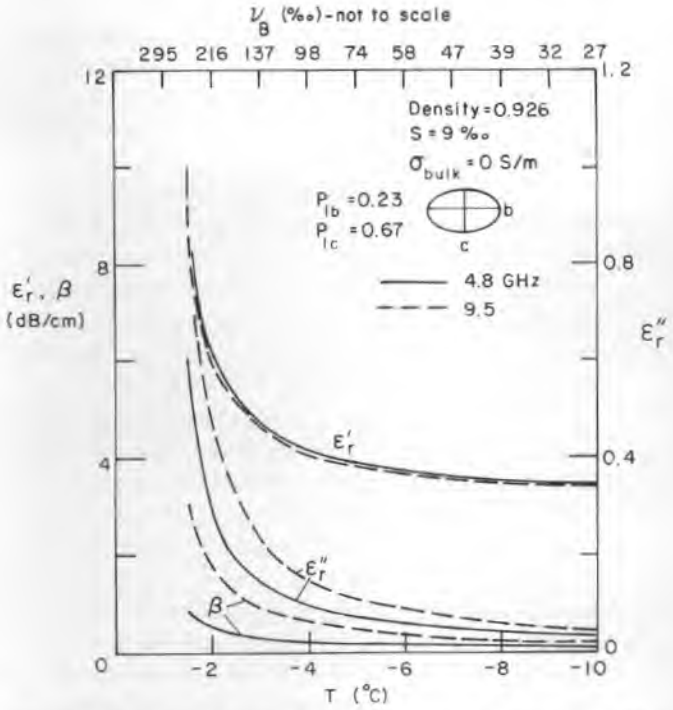

Figure 30. Dependency of ϵ_r^* and β upon temperature for a hypothetical model of high brine volume sea ice. The data are intended to model the behavior of freshly growing ice. The assumption of $\sigma_{bulk} = 0$ shows the inadequacy of the model in predicting observed attenuation rates (β).

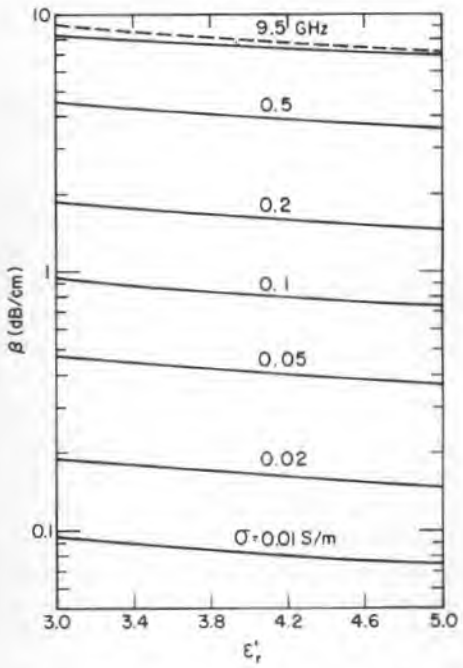

Figure 31. Attenuation rate vs dielectric constant for various values of conductivity σ at 4.75 and 9.50 GHz (broken curve). Only by σ = 1 S/m does the 9.50 GHz rate differ noticeably from that for 4.75 GHz so that d.c. conduction cannot be responsible for the increase in attenuation rates seen with increasing microwave frequency.

denced by the density values given in Table 1. Figure 30 shows that at any given brine volume, use of the in-situ sea ice density of 0.926 elevates all modeling ϵ_r' values for warming cycles by about 3% and ϵ_r'' values by 2.5% or less (compare with Fig. 28c for slab 85-3). Therefore, despite the loss of brine, the dielectric permittivity values are believed to simulate well the properties as they exist in-situ.

A modification of this model (as well as other scattering models) based on inclusion interaction was examined in hopes of obtaining a better match of ϵ_r' to the warming curves of slabs 85-2 and 3. A measured, average dendrite length of 2.41 mm and a width of 0.03 mm were used for the ellipsoidal axial lengths in the b and c directions respectively to account for the close spacing of the inclusions along dendritic planes. These dimensions give a very small value to P_{lb} (≈ 0.01) which results in ϵ_r' giving a good match for $T < -9°$ but with errors approaching 30% in excess of our data as T approaches -2°. Unfortunately, ϵ_r'' exceeds our data by an order of magnitude and is, thus, far in excess of all other reported data at these frequencies. A theory based on multiple scattering in a dense medium (Tsang and Kong 1980) gives even less loss than that predicted by linear independent scattering theory (e.g. Kerr 1965) which gives the right frequency dependence but values that are at least an order of magnitude too low. More recent developments by Stogryn (1985) may hold more promise.

SUMMARY AND CONCLUSIONS

The ϵ_r' results for the seven saline slabs at two frequencies all show a dependence on v_B that is linear to about 50‰ and then nonlinear above 50‰, with progressively greater variance. Comparison of warming and cooling values revealed that the replacement of brine with air could have lowered ϵ_r' by as much as 6% at any one value of v_B, while changes due to any redistribution of brine inclu-

sions were probably not significant. The 1983–84 slab and 1984–85 in-situ data for ϵ_r'' are consistent, as they generally show an increase with increasing v_B. These data were consistent with only a few isolated values of ϵ_r'' for the 1984–85 slabs. Slabs removed from seeded and unseeded sections of the same ice sheets (these slabs differ mainly in the size of their columnar crystals) showed similar dielectric properties. Modeling studies suggest that in-situ dielectric values at $v_B < 100‰$ were probably no more than about 3% greater than the warming values measured for the removed slabs.

Coupling between brine inclusions and the electric field vector is given for causing the behavior of ϵ_r' at microwave frequencies as has been proposed and formulated by others (Tinga et al. 1973, Vant et al. 1978). However, this coupling must result mainly from an average inclusion elongation in the horizontal plane as was observed, not from an angular displacement of the dendritic planes relative to the (usually vertical) direction of wave propagation as has been previously hypothesized (Vant et al. 1978) at least in first-year sea ice. The two concepts are mathematically similar because the coupling effects of vertically tilted ellipses come from their projection onto the horizontal plane, and the theory does not specify absolute ellipsoid size, only semi-axis ratios. Consequently, there is much leeway in the theory to account for brine inclusion shape and orientation, while ice and brine properties are well documented (Glen and Paren 1975, Stogryn and Desargent 1985). No present theory considers any effect due to the absolute vertical length of the brine inclusions.

The choice of a particular geometry for the brine pockets necessitated neglect of interactions between inclusions higher than first order in the mixing theory (Tinga et al. 1973). This cannot be correct for first-year ice, where brine-filled inclusions located between the dendritic plates of the crystals can be spaced closer than an inclusion length and often appear interconnected. Consequently, the model best fits the ϵ_r' data in Figure 28 for the more desalinated or multi-year type ice, which contains more brine inclusions that have drained. This does not suggest that electrical permeability in the horizontal plane can decrease with thermal modification, only that there is less dipolar interaction between the inclusions. Therefore, the role of conductivity should be more thoroughly investigated, especially as a function of aging which affects permeability. This is being done on artificial sheets grown during 1986 (Arcone 1987). Field measurements of conductive and microwave properties of anisotropic ice would be of immense help in clarifying the role of various loss mechanisms. Campbell and Orange (1974), Kovacs and Morey (1978), and Arcone and Delaney (1979) discuss VHF observations.

The mixing theory used in this research can also be used to predict some frequency dependence as was measured by Vant et al. (1978). This theory predicts that ϵ_r' will slowly decrease with increasing frequency throughout the microwave and millimeter wave region, which is consistent with the comparison of ϵ_r' at 9.50 and 4.80 GHz seen in Figure 26. Above 10 GHz, ϵ_r' will generally lie between 3.2 and 4.0 at brine volumes up to $100‰$. Values of ϵ_r'' at frequencies above 20 GHz cannot be predicted with this theory because scattering occurs when in-situ wavelengths approach the circumferential dimension of a brine pocket, which can be several millimeters judging by the data in Table 3. Quasi-optical, free-space transmission techniques, such as done here, or Fabret-Perot interferometry could be used for measurements at higher frequencies, but highly collimated beams would sample a smaller volume of ice than did our system, and slabs would have to be much thinner than 8 cm to obtain significant values of ϵ_r''. Sensing of a small sample volume is thought to cause the ranges of values seen about our data points. These ranges may enlarge at higher frequencies given the difficulties of precise realignment over a long period of storage and measurement.

The current experiments were limited to congelation ice. However, future measurements should include tests on granular or simulated frazil ice. Frazil ice occurs typically in the top layer of arctic sea ice and its dielectric properties may significantly differ from those of congelation ice because of major differences in the structural makeup of the two ice types. Since frazil ice is a major component of the earliest-formed sea ice, its microwave dielectric properties are of obvious importance to the remote sensing community.

LITERATURE CITED

Addison, J.R. (1969) Electrical properties of saline ice. *Journal of Applied Physics,* **40**(8): 3105–3114.

Addison, J.R. (1970) Electrical relaxation in saline ice. *Journal of Applied Physics,* **41**(1): 54–63.

Arcone, S. (1987) DC resistivity measurements of model saline ice sheets. *IEEE Transactions on Geoscience and Remote Sensing* (to appear November 1987).

Arcone, S.A. and A.J. Delaney (1979) HF to VHF radiofrequency polarization studies in sea ice at Pt. Barrow, Alaska. In *Proceedings of the International Workshop on Remote Estimation of Sea Ice Thickness, St. Johns, Newfoundland.* St. Johns, Newfoundland: Memorial University, C-CORE publication 80-5.

Arcone, S.A. and S.G. McGrew (1985) Dielectric properties at 4.75 GHz of saline ice slabs. In *1985 International Geoscience and Remote Sensing Symposium (IGARSS '85) Digest.* Amherst, Massachusetts: IEEE Catalog no. 85CH2162-6.

Assur, A. (1960) Composition of sea ice and its tensile strength. USA Cold Regions Research and Engineering Laboratory, Research Report 44.

Bogorodsky, V.V. (1979) Electromagnetic properties of sea ice. In *Proceedings of the International Workshop on Remote Estimation of Sea Ice Thickness, St. Johns, Newfoundland.* St. Johns, Newfoundland: Memorial University, C-CORE publication 80-5.

Bogorodsky, V.V. and G.P. Khoklov (1975) Interpretation of experimental data while measuring nonuniform samples of sea ice at centimeter wavelengths. Arctic and Antarctic Science Research Institute (AANSII), Leningrad, Report 324.

Campbell, K.J. and A.S. Orange (1974) The electrical anisotropy of sea ice in the horizontal plane. *Journal of Geophysical Research,* **79**(33): 5059–5063.

Collin, R.E. (1960) *Field Theory of Guided Waves.* New York: McGraw Hill.

Frankenstein, G. and R. Garner (1967) Equations for determining the brine volume of sea ice from -0.5° to -22.9°C. *Journal of Glaciology,* **6**(48): 943–944.

Glen, J.W. and J.G. Paren (1975) The electrical properties of snow and ice. *Journal of Glaciology,* **15**(73): 15–38.

Gow, A.J. (1985) Simulated sea ice used for correlating the electrical properties of the ice with its structural and salinity characteristics. In *1985 International Geoscience and Remote Sensing Symposium (IGARSS '85) Digest.* Amherst, Massachusetts: IEEE Catalog no. 85CH2162-6.

Gow, A.J. (1986) Orientation textures in ice sheets of quietly frozen lakes. *Journal of Crystal Growth,* **74**: 247–258.

Gow, A.J. and W.F. Weeks (1977) The internal structure of fast ice near Narwhal Island, Beaufort Sea, Alaska. USA Cold Regions Research and Engineering Laboratory, CRREL Report 77-29, p. 8.

Grenfell, T.C. and J.C. Comiso (1986) Multifrequency passive microwave observations of first-year sea ice grown in a tank. *IEEE Transactions of Geoscience and Remote Sensing,* **GE24**(6): 826–831.

Hallikainen, M. (1980) Dielectric properties and passive remote sensing of low-salinity sea ice at UHF frequencies. In *Acta Polytechnica Scandinavica.* Helsinki, Finland: Finnish Academy of Sciences, Electonic Engineering Series No. 5.

Kerr, D.E. (Ed.) (1965) *The Propagation of Short Radio Waves.* New York: Dover Publications.

Kovacs, A. and R.M. Morey (1978) Radar anisotropy of sea ice due to preferred azimuthal orientation of the horizontal c-axes of ice crystals. *Journal of Geophysical Research,* **83**(C12): 6037–6046.

Morey, R.M., A. Kovacs and G.F.N. Cox (1984) Electromagnetic properties of sea ice. *Cold Regions Science and Technology,* **9**: 53–74.

Osborn, J.A. (1945) Demagnetizing factors of the general ellipsoid. *Physics Review,* **67**(11 and 12): 351–357.

Sillars, R.W. (1937) The properties of a dielectric containing semi-conducting particles of various shapes. *Journal of the Institute of Electrical Engineering (London),* **80**: 378–394.

Stogryn, A. (1985) An analysis of the tensor dielectric constant of sea ice at microwave frequencies. Aerojet Electrosystems Company, Azusa, California, Report 7975.

Stogryn, A. and G. Desargent (1985) The dielectric properties of brine in sea ice at microwave frequencies. *IEEE Transactions on Antennas and Propagation,* **AP-33**(5): 40–48.

Swift, C.T., D.C. DeHority, A. Tanner and R.E. McIntosh (1986) Passive microwave emission from saline ice at C-band during the growth phase. *IEEE Transactions on Geoscience and Remote Sensing,* **GE24**(6): 840–848.

Taylor, L.S. (1965) Dielectric properties of mixtures. *IEEE Transactions on Antennas and Propagation,* **AP-13**(4): 943–947.

Taylor, L.S. (1966) Dielectric loaded with anisotropic materials. *IEEE Transactions on Antennas and Propagation,* **AP-14**(4): 669–670.

Thyssen, F., H. Kohnen, M.V. Cowan and G.W. Timco (1974) DC resistivity measurements on the sea ice near Pond Inlet, N.W.T. (Baffin Island). *Polarforschung,* **J44**: 117–126.

Timco, G.W. (1979) An analysis of the in-situ resistivity of sea ice in terms of its microstructure. *Journal of Glaciology,* **22**(88): 461–471.

Tinga, W.R., W.A.G. Voss and D.F. Blossey (1973) Generalized approach to multi-phase dielectric mixture theory. *Journal of Applied Physics,* **44**(9).

Tsang, L. and J.A. Kong (1980) Multiple scatter-

ing of electromagnetic waves by random distributions of discrete scatterers with coherent potential and quantum mechanical formulism. *Journal of Applied Physics,* **51**(7): 3465–3485.

Vant, M.R., R.O. Ramseier and V. Makios (1978) The complex dielectric constant of sea ice at frequencies in the range 0.1 to 40 GHz. *Journal of Applied Physics,* **49**(3): 1264–1280.

Ward, S.H. and D.C. Fraser (1967) Conduction of electricity in rocks. In *Mining Geophysics.* Tulsa, Oklahoma: Society of Exploratory Geophysics, Vol. II, p. 205.

Weeks, W.F. and S.F. Ackley (1982) The growth, structure and properties of sea ice. USA Cold Regions Research and Engineering Laboratory, Monograph 82-1, p. 130.

APPENDIX A: DIELECTRIC MIXING MODEL OF SEA ICE

This model was originally proposed by Taylor (1965, 1966), extended by Tinga et al. (1973) and adapted to sea ice by Vant et al. (1978). Tinga et al.'s model solves for the dielectric permittivity of a mixture of two or three different dielectrics consisting of a host medium (ϵ_1), which contains any density of inclusions in the form of concentric ellipsoids (ϵ_2, ϵ_3) that are smaller than any wavelength imposed upon the medium. Therefore, static theory (Laplace's equation) is used to find the resulting electric field within the ellipsoids (and consequently, the relative permittivity) due to an impressed, constant electric field across the material. The individual volumes of the ellipsoids are of no consequence because of the wavelength-size criterion. The parameters of importance are the relative volume of the inclusions, their axial ratios as expressed through the ellipsoidal depolarization coefficients, and the orientation of the ellipsoid axes relative to the impressed electric field.

The application to sea ice as adapted by Vant et al. (1978) gives the mixture dielectric constant ϵ_{av} as

$$\epsilon_{av} = \epsilon_1 + \frac{V_2}{V_1} \frac{\epsilon_1(\epsilon_2 - \epsilon_1)}{[-(V_2/V_1)P_1(\epsilon_2 - \epsilon_1) + P_2(\epsilon_2 - \epsilon_1) + \epsilon_1]} \tag{A1}$$

where V_1 and V_2 are the volume fractions of the host medium (ice) and ellipsoidal inclusions (brine) respectively. The quantities P_1, P_2 are the principal depolarization coefficients for the ellipsoidal directions parallel to the applied electric field and depend only on the semi-axis ratios. These quantities are equal for any particular direction because the sample volume of the host material surrounding the brine inclusion, and in which the internal electrical field is calculated, is assumed to be bounded by an ellipsoidal surface confocal with the inclusion ellipsoid. According to Tinga et al. (1973), the use of this additional ellipsoidal surface accounts for inclusion interactions to first order and thus permits application of eq A1 to materials with a high density of inclusions.

Equation A1 can be reiterated to include air (ϵ_2) inside the host medium (ϵ_{av}) to give a new value to ϵ_{av} because air bubbles are not confocal with brine ellipsoids. The calculations used to produce the curves in Figure 28 assumed spherical air bubbles as observed in the thin sections. A further refinement (not utilized here) would be to assume some of the air pockets are ellipsoidal because of any drained brine. However, this would offer only a minor change in ϵ_r^* values.

Vant et al. (1978) offer further refinements by utilizing the extraordinary ray formula from optical crystallography to compute the dielectric constant $\epsilon_{av,\theta}$ for sea ice in which the long axis of the brine ellipsoid is tilted at an angle θ from vertical (i.e. the direction of incident wave propagation):

$$\frac{1}{\epsilon_{av,\theta}} = \frac{\sin^2\theta}{\epsilon_{av,a}} + \frac{\cos^2\theta}{\epsilon_{av,b}} \tag{A2}$$

where a and b refer to the long and short semi-axis lengths of the vertical ellipsoid, respectively (c is the second, short semi-axis of Vant et al. (1978) where $c = b$). They then assume random orientation in azimuth of the electric field with respect to the ellipsoids, to give an effective, overall dielectric constant ϵ_{eff} such that

$$\epsilon_{eff} = (\epsilon_{av,b} + \epsilon_{av,\theta})/2. \tag{A3}$$

It is proposed here that $P_1 (= P_2)$ of eq A1 correspond to either the b or c ellipsoid direction in the horizontal plane and that eq A3 be supplemented with the loss term

$$-i\,\sigma_{bulk}/\omega\epsilon_0$$

where σ_{bulk} is the bulk d.c. conductivity of the ice. The reader is referred to Timco (1979) for a possible derivation of σ_{bulk} from the constituent material properties. In addition, eq A2 is disregarded for the main bulk of first-year type ice because θ is on the average close to 0°. Equation A3 is then simply altered to

$$\epsilon_{eff} = (\epsilon_{av,c} + \epsilon_{av,b})/2 - i\,\sigma_{bulk}/\omega\epsilon_0 \tag{A4}$$

to account for the random orientation in the horizontal plane.

In keeping with the ellipsoidal notation of Vant et al. (1978), our a axis is in the vertical direction while b and c are in the horizontal directions. The depolarization coefficients P_{1b} and P_{1c} in the b and c directions, respectively, were taken from the graphs of Osborn (1945) because closed form integral solutions are not available for cases where the three axes are unequal. Use of these tables requires a simple redefinition of a, b and c if the measured axes do not always decrease in length in the same sequence. The depolarization coefficients used in eq A1 are normalized by 4π as shown by Tinga et al. (1973).